Supplementary Material for

Tunable porous nanoallotropes prepared by post-assembly etching of binary nanoparticle superlattices

Thumu Udayabhaskararao, Thomas Altantzis, Lothar Houben, Marc Coronado-Puchau, Judith Langer, Ronit Popovitz-Biro, Luis M. Liz-Marzán, Lela Vuković, Petr Král, Sara Bals, Rafal Klajn*

*Corresponding author. Email: rafal.klajn@weizmann.ac.il

Published 27 October 2017, *Science* **358**, 514 (2017)
DOI: 10.1126/science.aan6046

This PDF file includes:

Materials and Methods

Colloidal synthesis of nanoparticles (NPs)

Synthesis of 5.2±0.4 nm gold nanoparticles: monodisperse 5.2 nm dodecanethiol-stabilized Au NPs were prepared based on a previously reported procedure (*31*). Specifically, 65 mg of $HAuCl_4 \cdot 3H_2O$ and 202 mg of didodecyldimethylammonium bromide (DDAB) were dissolved in 20 mL of toluene (with sonication). In a separate vial, 700 mg of $NaBH_4$ was dissolved in 2 mL of deionized water. Next, 100 μL of the borohydride solution was injected into the $AuCl_4^-$ solution with vigorous stirring. Neat dodecanethiol (DDT) (1.6 mL) was added and the mixture was stirred for an additional 2 h. The resulting solution was mixed with 20 mL of ethanol and DDT-passivated Au NPs were precipitated by centrifugation, collected, dried under vacuum, and then redispersed in a mixture of 20 mL of toluene and 1.6 mL of DDT (with sonication). Thus obtained solution was refluxed for 3 h under a nitrogen atmosphere (digestive ripening (*32*)). The solution was allowed to cool down and the NPs were precipitated with ethanol (with centrifugation). The precipitate was collected, dried under vacuum and redispersed in 5 mL of pure toluene. The resulting solution was centrifuged (5 min at 7,000 rpm) to remove any large particles; the upper layer was collected, dried under vacuum, and finally redispersed in pure hexane. TEM images of the resulting NPs are shown in fig. S1, *left*.

Synthesis of 5.2±0.4 nm gold nanoparticles: The more polydisperse particles were obtained by storing the above 5.2±0.4 nm Au NPs in hexane for three months at room temperature. TEM images of the resulting NPs are shown in fig. S1, *center*.

Synthesis of 3.0±0.3 nm gold nanoparticles: Monodisperse 3.0 nm dodecanethiol-stabilized Au NPs were prepared by modifying a previously reported procedure (*33*). First, a solution of 98.5 mg of $HAuCl_4 \cdot 3H_2O$ and 10 mL of oleylamine (OLA) in 10 mL of hexane was prepared and brought to 15 °C using a thermostatic bath (with magnetic stirring). To the resulting orange mixture, a solution of *t*-butylamine-borane complex (44 mg) in 1 mL of hexane containing 1 mL of OLA was injected under a nitrogen flow. The mixture turned purple within 5 s and was allowed to react at 15 °C for an additional hour before ethanol (60 mL) was added to induce the precipitation of the NPs. The NPs were collected by centrifugation (6,000 rpm for 5 min), washed with ethanol, dried, and redispersed in pure toluene. The particles were functionalized with DDT by place-exchange reaction as reported previously (*34*). Specifically, 10 eq of DDT (per surface-bound OLA) were added to the NPs and the mixture was shaken on an orbital shaker for 12 hours. The DDT-passivated NPs were purified from excess DDT by precipitation and copious washing with methanol, and finally redispersed in pure hexane. TEM images of the resulting NPs are shown in fig. S1, *right*.

Synthesis of iron oxide nanoparticles: Iron oxide (Fe_3O_4) NPs (8.4±0.4 nm, 10.6±0.6 nm, 13.0±0.6 nm) were synthesized by modifying a previously reported literature procedure (*35*). First, iron(III) oleate was prepared as follows: to a solvent mixture composed of *i*) 60 mL of distilled water, *ii*) 80 mL of ethanol and *iii*) 140 mL of hexane were added sodium oleate (36.5 g; 120 mmol) (TCI, >97%; note that the high purity of sodium oleate was critical for reproducible synthesis of high-quality, monodisperse Fe_3O_4 NPs) and $FeCl_3 \cdot 6H_2O$ (10.8 g; 40 mmol) (Alfa Aesar, 98%) and the resulting mixture was vigorously stirred at room temperature until a homogeneous solution was obtained. The mixture was then heated with vigorous stirring under a nitrogen atmosphere at 70 °C for 4 hr. The solution was cooled

down to room temperature and the upper phase (dark-red color) was collected using a separatory funnel and washed three times with distilled water. The resulting dark-red solution of iron oleate in hexane was dried over anhydrous magnesium sulfate. The solvent was evaporated *in vacuo* at 70 °C, resulting in a brown waxy solid. Next, iron oleate (1.60 g; 1.78 mmol) was dissolved in 25 mL of 1-octadecene (Aldrich, 90%) and a given amount of oleic acid (Alfa Aesar, 90%) was added. The amount of oleic acid controlled the diameter of the resulting NPs: to obtain 8.4 nm, 10.6 nm, and 13.0 nm Fe_3O_4 NPs, we added 1.1 g (3.90 mmol), 0.99 g (3.55 mmol), and 0.86 g (0.30 mmol) of oleic acid, respectively. The reaction mixture was initially heated to 80 °C under reduced pressure for 30 min in order to remove any low-boiling liquids, and subsequently heated up to T = 310 °C at a constant heating rate of 3 °C per min, and it was stirred at this temperature for 30 min under a nitrogen atmosphere. The heating mantle was removed and the reaction mixture was allowed to cool down to room temperature. Nanoparticles were purified by precipitating with a mixture of solvents composed of hexane, isopropanol, and acetone ($v/v/v$ = 1:2:2). The transparent supernatant was discarded and the solids were washed with a hexane-acetone mixture (v/v = 1:2). Residual solvent was evaporated under reduced pressure, resulting in monodisperse Fe_3O_4 nanoparticles as a black solid. The resulting oleate-passivated NPs were readily soluble in hexane. TEM images of as-prepared Fe_3O_4 NPs are shown in fig. S2.

Fabrication and characterization of binary nanoparticle superlattices (BNSLs) and non-close-packed (NCP) NP arrays

Self-assembly of BNSLs: BNSLs were prepared based on a previously reported method (*20*). Hexane solutions of Au and Fe_3O_4 NPs were mixed to afford an Au/Fe_3O_4 particle ratio between 0.5 and 10. The resulting solution was diluted with pure hexane such that the total NP concentration was 0.1-1 mg/mL. Next, 10 μL of the diluted solution was dropcasted onto several mL of diethylene glycol (DEG) inside a Teflon well. The well was covered with a glass slide and hexane was allowed to evaporate within ca. 15 min. The resulting BNSLs were transferred onto carbon-coated copper grids or Si wafers for inspection by TEM and SEM, respectively.

Selective etching of BNSLs: BNSLs obtained at the DEG-air interface were transferred onto carbon-coated substrates using a lift-off technique. We worked with both commercial and homemade substrates. Homemade substrates were prepared as follows: copper grids (300- or 400-mesh) were covered with a thin film of nitrocellulose, prepared by spreading 3-4 drops of 1% solution of nitrocellulose in amyl acetate on the surface of water (in a crystallizing dish). The dried grids were then coated with a thin layer of amorphous carbon using an Edwards evaporator. Alternatively, commercial substrates (copper grids coated with amorphous carbon supported on Formvar; Electron Microscopy Sciences FCF400-CU-50) could be used. Residual DEG was removed by placing the substrates under high vacuum. The dried grids were subjected to heating (70 ºC in an oven, typically for 1-2 hr), placed inside a vacuum chamber of a TEM (we worked with a Philips CM120 Super Twin TEM operated at 120 kV), and exposed to the electron beam for 10-20 min in a low-magnification mode (such that the entire grid was exposed to the beam at once). The grids were removed from the TEM and placed in an etchant solution. For a selective removal of Fe_3O_4 NPs, we used a 3.5 M aqueous solution of HCl (etching time: 10-60 sec). For a selective removal of Au NPs, a 0.1 M aqueous solution of KCN was used (etching time:

30-60 min) (for etching of Au, pre-exposure to the electron beam was not required). The grids were rinsed with deionized water and finally dried under high vacuum.

Supplementary Text

Modeling of BNSLs at the liquid-air interface

We used classical atomistic molecular dynamics (MD) simulations to examine the principles governing the self-assembly of NPs at liquid-air interfaces. We determined the immersion of individual particles, calculated the energies associated with the immersion process, and found the NP-NP binding energies in vacuum and at the liquid-air interfaces.

Molecular dynamics simulations: Atomistic models of a dodecanethiol-covered Au NP (core diameter ~5 nm, 380 ligands) and an oleate-covered Fe_3O_4 NP (core diameter ~10 nm, 1270 ligands) were prepared (*40-42*). For simplicity, both types of NPs were modeled as hollow shells formed by atomic monolayers of icosahedral shapes with randomly attached ligands. These NPs were modeled alone or in pairs at the liquid-air interface (where liquid = diethylene glycol (DEG), ethylene glycol (EG), and water) and at the DEG-hexane interface. The systems contained between 30,000 and 700,000 atoms and were simulated for 15-100 nanoseconds.

MD simulations were performed with NAMD2.11 software (*43*). NP ligands and solvents were described with the generalized CHARMM force field (*44, 45*), and the parameters were determined via the CGenFF ParamChem web interface (*46, 47*). The NP core atom parameters had little influence on the NP-solvent and NP-NP interactions since they were densely covered by NP ligands. In all the simulations, the particle-mesh Ewald (PME) method (*48*) was used for evaluation of long-range Coulomb interactions. The time step was set to 2.0 fs, and long-range interactions were evaluated every one (van der Waals) or two (Coulombic) time steps. After 2,000 steps of minimization, solvent molecules were equilibrated for 1 ns around the NPs, which were restrained using harmonic forces with a spring constant of 1 kcal/(mol $Å^2$). Then, the systems were equilibrated by MD simulations without restraints. The simulations were performed in the NpT (DEG-hexane interface; p = 1 bar) and NVT ensembles (all vacuum interfaces) at a constant temperature of T = 310 K and a Langevin constant of $\gamma_{Lang} = 0.01$ ps^{-1}.In order to quantify the binding affinity of NPs to different liquids and their interfaces, NAMD Energy plugin in VMD (*49*) was employed. Images of the simulated systems were also prepared with VMD. All the analyses were performed during second halves of production runs.

Gibbs free energy calculations: Gibbs free energy of binding between a single DEG molecule and a gold NP in vacuum was determined in umbrella sampling (US) calculations (*50*). The reaction coordinate, defined as the distance between the center of mass of a DEG molecule and the NP core center was partitioned into 17 windows of a 1-Å width. Confinement potentials were introduced in the form of harmonic restraints with a force constant k = 3 kcal/(mol $Å^2$) and each window was run for 10 ns as the DEG molecule quickly sampled its binding conformations. The weighted histogram analysis method (WHAM) was used to reconstruct the PMF, and Monte Carlo bootstrap error analysis was performed also with the WHAM algorithm (with num_MC_trials set to 5) (*51, 52*). The histograms of the US windows used to reconstruct the PMF were examined, and had an appropriate overlap.

Single NPs at interfaces: In the first set of simulations, individual Au and Fe_3O_4 NPs (described above) were placed at midpoints of the DEG-hexane, DEG-vacuum, EG-vacuum, and water-vacuum interfaces. Figure S48 shows that during the equilibration simulations

NPs adjusted to their preferred solvation levels at these interfaces. At the DEG-hexane interface, Au NPs and Fe_3O_4 NPs immersed into hexane within 50-70 nanoseconds (fig. S48A). At the DEG-vacuum and EG-vacuum interfaces, both Au NPs and Fe_3O_4 NPs remained about halfway immersed in the liquids during 50 nanoseconds of simulations (figs. S48, B and C). At the water-vacuum interface, both types of NPs shifted towards vacuum within 15 nanoseconds, thus reducing the ligand-water contact area (fig. S48D).

Table S1 provides the coupling energies between individual Au or Fe_3O_4 NPs and the underlying liquids (DEG, EG, and water). The coupling energies were calculated by the VMD plugin that provides the sum of van der Waals (vdW) and Coulombic coupling energies between the NP ligands and the solvent molecules (determined by parameters in the CHARMM force field), which are related to the respective forces (vdW: attractive; steric: repulsive; Coulombic: both attractive and repulsive) acting between the system's components. These energies only represent partial (see below) enthalpy components in the Gibbs free energies of NPs binding to the underlying liquids. For simplicity, we can assume that the Gibbs free energies are proportional to these enthalpies with a common factor. Simplified calculations performed below provide an estimate that the Gibbs free energies can be about 2-3 times smaller than these enthalpies, due to the molecular confinement (entropic effects).

The calculations below show that the coupling energies of Au or Fe_3O_4 NPs to DEG are roughly proportional to the immersed areas of these NPs. Therefore, during the self-assembly processes, these NPs should have the ability to displace each other from the surface of DEG. In the case of EG, however, the coupling energies are not proportional to the immersed surfaces of NPs; rather, EG favors interactions with Fe_3O_4 NPs. Therefore, these NPs should dominate at the surface of EG and hence disrupt the NP co-assembly processes. These considerations are in agreement with previous experimental studies, which found that DEG is superior to EG in the formation of BNSLs (*26, 27*).

DEG: $$\frac{E_{Fe_3O_4}}{E_{Au}} = 3.67 \approx \frac{A_{Fe_3O_4}}{A_{Au}} = \frac{r^2_{Fe_3O_4}}{r^2_{Au}} = \frac{6.8^2}{3.6^2} = 3.57$$

EG: $$\frac{E_{Fe_3O_4}}{E_{Au}} = 4.38 > \frac{A_{Fe_3O_4}}{A_{Au}} = \frac{r^2_{Fe_3O_4}}{r^2_{Au}} = \frac{6.8^2}{3.6^2} = 3.57$$

NP pairs at the DEG-vacuum interface: In the second set of simulations, coupling energies of pairs of NPs (Au-Au, Au-Fe_3O_4, and Fe_3O_4-Fe_3O_4) (evaluated by VMD) were examined in vacuum and at the DEG-vacuum interface. Initially, the NPs were placed close to each other. After 30-40 ns of simulations, the separation between the NPs decreased both in vacuum and at the DEG-vacuum interface as the ligands on the different NPs reached each other and started to interact very strongly. At the DEG-vacuum interface, the NPs immersion levels remained similar as at the beginning of the simulations (about half-immersed).

In table S2, we provide the NP-NP coupling energies (enthalpies), calculated as in table S1, for the cases shown in fig. S49. One can see that the interparticle interactions at the DEG-vacuum interface (–200 to –440 kcal/mol) are weaker than in vacuum (–250 to –480 kcal/mol) since the ligand-ligand coupling between the neighboring NPs is partly replaced by the ligand-DEG coupling. This weakening of the NP-NP coupling for submerging

NPs explains why the relatively weak bulk vdW coupling between the NP cores (~ –5 kcal/mol) becomes important only for NPs fully immersed in DEG. Indeed, if the strengths of the ligand-DEG coupling and the ligand-ligand coupling were similar, the ligands would not contribute to the binding of submerged NPs (i.e., the ligand-related enthalpic component in the Gibbs free energy of NP-NP binding would be ~0). These results also show that i) the evaporation of hexane dramatically increases the NP-NP coupling (it "locks" the NPs) and ii) the NP-liquid coupling can become dominant owing to the large contact area formed between DEG and half-submerged NPs.

NPs favor semi-immersed positions at the DEG-vacuum interface: In order to explain why NPs assume semi-immersed positions at the DEG-vacuum interface (see figs. S48 and S49), we examined the major energetic contributions to NP solvation. When a NP immerses in a liquid, it creates a cavity with an excess surface area of the solvent, A_{excess}. The Gibbs free energy cost, G_1, to create the additional surface area in DEG can be estimated as, $G_1 = \gamma A_{excess} = \gamma (A_{immersed} - A_{slice}) = \gamma (2\pi Rh - \pi(2Rh - h^2))$, where γ is the surface tension of DEG (~45 dyne/cm), surface areas are defined as in fig. S50A, R is the radius of the ligand-functionalized Au NP (i.e., NP core + ligand shell) estimated as 3.5 nm, and h is the immersion height of the NP. The free energy cost of submerging a gold NP, G_1, as a function of NP immersion depth, h, is shown as the red line in Fig. 2L.

The Gibbs free energy cost of creating the cavity is balanced by favorable interactions between the NP ligands and the solvent, which can be estimated as $G_2 = G° A_{immersed}$, where G° is the free energy per unit area of binding between DEG and a gold NP, and $A_{immersed}$ is shown schematically in fig. S50A. For a dodecanethiol-covered Au NP, we can estimate G° ~ –7 kcal/(mol nm^2) from the Gibbs free energy of binding of a single DEG molecule to Au NP, ΔG_{bind} = –3.5 kcal/mol, and the approximate contact area that a DEG molecule has with the Au NP surface (0.5 nm^2) (fig. S50B). The interaction energy, G_2, as a function of the immersion height, h, is shown as the blue line in Fig. 2L. The Gibbs free energy, G_2, is about 2-3 times smaller than the energy (enthalpy), E_2, directly obtained from our simulations (VMD), highlighting the importance of the entropic contribution.

By adding the two Gibbs free energy contributions, G_1 and G_2, we obtain the total free energy, G, as a function of the immersion height, h, which is shown as the thick black line in Fig. 2L. The energy cost, G_1, increases and the favorable free energy of DEG-NP binding, G_2, decreases as the NP immerses into DEG. Overall, the total free energy develops a minimum at an approximately half-immersed position of the Au NP in DEG, as observed in equilibrium MD simulations.

BNSLs prepared at DEG/water-air interfaces: To further confirm the unique role of DEG in templating the formation of well-ordered BNSLs, we studied self-assembly of a 1:1 mixture of ~5 nm Au and ~10 nm Fe_3O_4 NPs in the presence of several DEG/water mixtures. We found that the presence of as little as 10% (*v*/*v*) water in the underlying liquid had a profound deleterious effect on the quality of the BNSL obtained. Instead of a well-defined NaCl-type monolayer (fig. S51A), we observed the formation of a ~1:1 mixture of the monolayer and the "type II" bilayer (fig. S51B). The formation of bilayers from NPs used in amounts expected to give rise to submonolayer coverage of the underlying liquid indicates a weaker coupling to the liquid and consequently a greater contribution of the NP-NP coupling. This effect was more pronounced in the presence of 25% water, where we found the formation of both types of NaCl-type bilayers, in addition to thicker BNSLs (fig. S51C). A small fraction of monolayer coverage was still present. When self-assembly took

place on a 1:1 (*v*/*v*) DEG-water mixture, no monolayers could be found; instead, thick arrays comprising several NP layers prevailed. Under these conditions, we also observed quasi-3D superlattices composed only of Fe_3O_4 NPs (fig. S51D). Overall, these observations are in agreement with the results of our simulations (fig. S48D), which show poor coupling of both types of NPs to water compared to DEG.

Lattice energies of BNSLs: The NP-NP interaction energies displayed in tables S1 and S2 can be used to estimate the lattice energies of the experimentally observed BNSLs. In these calculations, we first identify, based on the structural models shown below, the smallest repeating unit of each BNSL in the x-y plane (parallel to the liquid-air interface), which we define as the square whose corners are located to the centers of neighboring Fe_3O_4 NPs. In the z-direction (perpendicular to the liquid-air interface), we consider the initial two layers comprising Fe_3O_4 NPs. Then, we determine the number of Au and Fe_3O_4 NPs per unit cell that are in contact with DEG and multiply them by the NP-DEG coupling energies calculated above (table S1). Next, we determine the number of interparticle contact points (i.e., Au-Au, Au-Fe_3O_4, and Fe_3O_4-Fe_3O_4) within the unit cell and multiply them by the NP-NP interaction energies (table S2). For the base NP layers, the NP-NP interaction energies were divided by two since their bottom hemispheres were immersed in DEG and the NP-DEG interaction was separately accounted for (table S1). The obtained total energies (enthalpies) are listed in table S3 for three selected BNSLs sharing the same AB_4 bottom layer: AB_4 (i.e., $(\text{-}AB_4\text{-})_n$), AB_6 (i.e., $(\text{-}AB_4\text{-}B_2\text{-})_n$), and AB_{11} (i.e., $(\text{-}AB_4\text{-}B_7\text{-})_n$).

These considerations confirm the profound role of NP-DEG interactions on the stability of the resulting BNSLs. For example, the calculated coupling energy between the base layer of NPs in the AB_6-type BNSL and DEG is ~9,250 kcal/mol per unit cell, which is roughly an order of magnitude higher than the interaction energy between two adjacent monolayers of NPs (held together by four Au-Au contacts per unit cell; ~1,000 kcal/mol). Therefore, coupling to DEG plays a key role in controlling the formation of BNSLs. It should be emphasized, however, that these estimations are only approximate because: i) the NP-NP coupling energies were calculated for energy-minimized configurations of individual pairs of NPs, which does not reflect the situation in ensembles of multiple regularly arranged NPs; ii) both Au and Fe_3O_4 NPs used in the experiments were slightly polydisperse and their sizes and size ratios in the BNSLs could be different from the 5 nm and 10 nm sizes used in simulations.

Immersion of multilayer superlattices in DEG: Having established that monolayer-thick superlattices prefer to assume a half-immersed configuration at the DEG-vacuum interface, we studied the behavior of thicker superlattices by comparing the NP solvation forces with the gravitational forces acting on the superlattices. In particular, we were interested in determining at which value of superlattice thickness, its bottom layer becomes fully immersed.

Figure S52A shows our estimate of forces ($F_{immerse}$) associated with the immersion of a single dodecanethiol-functionalized Au NP (5 nm core + 1 nm ligand shell) positioned at the DEG-vacuum interface, derived from the free energy plot in Fig. 2L. The net force can be obtained by differentiating the free energy of NP solvation with respect to the immersion height. The free energy of solvation is defined as the sum of the energy cost term (creating the additional solvent interface upon immersion) and the favorable energy term (favorable ligand-DEG interactions upon NP immersion). When a nanoparticle is equilibrated at the DEG-vacuum interface, it is approximately half-immersed in DEG, so that a zero net force acts on it. When the NP is less than half immersed, a negative net vertical

force pulls it into the DEG. When, on the other hand, the NP is more than half immersed, a positive net vertical force pulls it out of DEG. We estimate that a vertical force of $F_{immerse} \sim 1.05 \cdot 10^{-9}$ N = 1.05 nN needs to be applied on this NP to fully immerse it into DEG. In contrast, a gravitational force acting on such a NP (mass of $\sim 2.2 \cdot 10^{-21}$ kg), $F_{grav} \sim -2.2 \cdot 10^{-20}$ N, is eleven orders of magnitude smaller. Although this force cannot lead to full immersion of the NP, a superlattice comprising many self-assembled NPs could have a different balance of forces.

Next, we examined the possible immersion of two model NP superlattices shown in fig. S52, B and C. First, we studied a cubic superlattice formed by spherical NPs (fig. S52B), similar to that observed experimentally. Here, DEG could fill the space between the NPs from the bottom superlattice layer. Therefore, each of these bottom-layer NPs opposes its immersion beyond the equilibrium (~half-immersion) level by a force that stabilizes the whole superlattice from immersion. The solvation forces acting on each of these spherical NPs can be determined using the approach shown in Fig. 2L and fig. S52A. For example, when a bottom-layer NP is 60% immersed in DEG, the opposing immersion force acting on it is $F_{immerse} \sim 2.18 \cdot 10^{-10}$ N (fig. S52A).

Based on the above estimates and assuming that the solvent level is flat, we determined the minimum forces needed to fully submerge the bottom (base) layers of superlattices formed by spherical NPs; see table S4. If the linear size of these base layers is increased by a factor of 10, the force required to submerge them is correspondingly increased by a factor of 100. By balancing $F_{immerse}$ with F_{grav} for each selected base layer, we can determine how tall the superlattices would need to be in order to submerge their bottom layer into the underlying DEG phase. The calculated height of the supported NP column is 70.6 m (even for 60% immersion) regardless of the base layer size. This large value shows that DEG practically cannot enter the superlattice, which behaves more like a compact body lacking pores. Therefore, we assume that superlattice immersion is controlled by the interactions of its side NPs with the solvent, which will more or less surround the immersed part of the superlattice, while staying within the first NP monolayer. Since the bottom-edge NPs might be more surrounded by the solvent, their NP-NP coupling should be weakened; therefore, these NPs might be released, resulting in a superlattice with smoother bottom edges.

To provide an estimate of the supporting forces, we can simplify the system by considering a more compact NP superlattice, where the solvent has limited access to the NPs. Such a case is shown in fig. S52C, where a superlattice is prepared from tightly packed cubic NPs (nanocubes, NCs) with an edge length of 7 nm (by analogy to spherical NPs having a 7 nm diameter). Here, the solvent is only present outside the superlattice, which means that only the external periphery of the superlattice contributes to its support against immersion. It turns out that when one of the NC facets is parallel to the solvent surface, the NCs can exist in two limiting solvation states, depending on the value of the ligand-DEG binding free energy. For ligand-DEG binding energies smaller than a certain threshold value, only the bottom NC facet interacts with DEG, whereas above the threshold value, the NCs become completely immersed, except for their top facets. This behavior is also valid for cubic assemblies of NCs shown in fig. S52C. In order to have individual NCs floating (i.e., not submerged), we considered in our calculations a model ligand-DEG free energy of binding, where $G° \sim -4.7$ kcal/(mol nm^2), corresponding to the value reported in fig. S50 and scaled by 2/3.

Table S5 shows the solvation and gravitational forces acting on supercubes of increasing sizes, formed by self-assembled NCs (fig. S52C), present at the DEG-vacuum interface. Here, as the edge length of the square base layer that faces the solvent increases by 10 times, the force required to immerse the system, $F_{immerse}$, increases by the same amount. By balancing $F_{immerse}$ with F_{grav} for each selected cubic base layer, we can determine how tall the superlattice should be to get immersed into DEG. For short edge lengths of the square base layer (< 0.5 μm), the superlattices must have a macroscopic height (> 0.68 m) to become immersed into DEG. In contrast, superlattices with much larger edge lengths of the square based layer (here, 500 μm) are immersed already when they reach mesoscale heights (680 μm). Based on tables S4 and S5, we expect that superlattices assembled from ~10^{11} NPs at the DEG-hexane interface are not able to immerse into DEG due to supporting NP-DEG coupling forces, but that larger systems would submerge like non-porous rigid bodies, depending on their overall sizes and densities (Archimedes' law).

Surface-enhanced Raman scattering

Surface-enhanced Raman scattering (SERS) measurements were performed with a confocal Raman microscope (InVia Reflex, Renishaw) equipped with a motorized scan stage, 633 nm laser excitation source (nominal output 16 mW), a corresponding laser line rejection filter (edge) and lens set, diffraction grating of 1,800 grooves/mm, and a Peltier-cooled CCD detector (size 512x1,024 pixels). The laser power was attenuated by means of neutral density filters in preset steps. Next, 3 mL of a 1 mM Malachite green ethanolic solution (freshly prepared from a 1 mM ethanolic stock) were dropcasted onto the TEM grids containing the three different porous nanoallotropes: *vac*$_1$Au$_1$, *vac*$_1$Au$_5$, and *vac*$_1$Au$_{11}$. Immediately after having been dried, the SERS spectra were measured in a 180º back-reflection geometry through a x100 magnification objective (Leica, numerical aperture 0.85) with an integration time of 10 s (extended scan mode) and a laser power of 40 mW at the samples at five different positions outside the copper grid. The collected spectra were averaged, smoothed (Savitsky-Golay method), and background-corrected using Wire 3.4 software.

The SERS activity of the three different substrates was measured by drop casting a solution of a dye Malachite green (MG) directly on the TEM grid. The characteristic SERS signals of MG (1617, 1594, 1393, 1366, 1298, 1218, 1173, 915, and 798 cm^{-1}) were obtained for structures *vac*$_1$Au$_{11}$ and *vac*$_1$Au$_5$, the former yielding ca. three times higher intensity. Interestingly, this intensity difference can be directly related to the number of available hotspots – analysis of tomography data revealed the presence of 28-32 nanogaps (defined as interparticle distances smaller than 1 nm) per 1,000 nm^2 of the *vac*$_1$Au$_5$ array, whereas for the *vac*$_1$Au$_{11}$ array, we found 78-85 nanogaps / 1,000 nm^2. As expected, sample *vac*$_1$Au$_1$ did not display any SERS signal owing to the significant separation distance between individual NPs, which prevents hotspot formation.

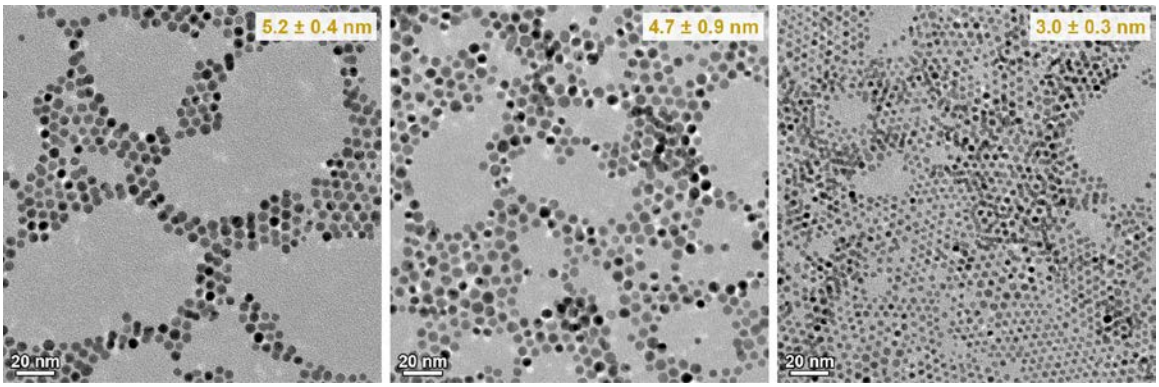

Fig. S1.

TEM images of gold nanoparticles used in the self-assembly experiments. To acquire TEM images, we used a Philips CM120 Super Twin TEM operated at 120 kV unless indicated otherwise.

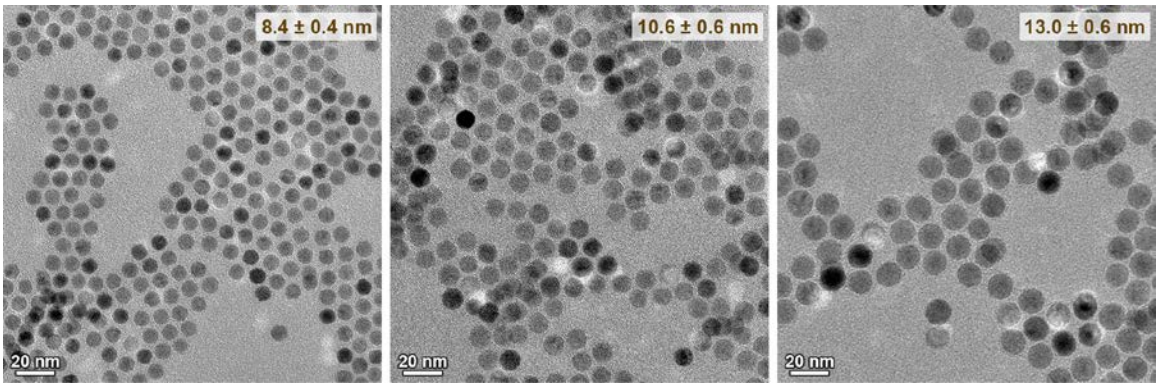

Fig. S2.
TEM images of iron oxide nanoparticles used in the self-assembly experiments.

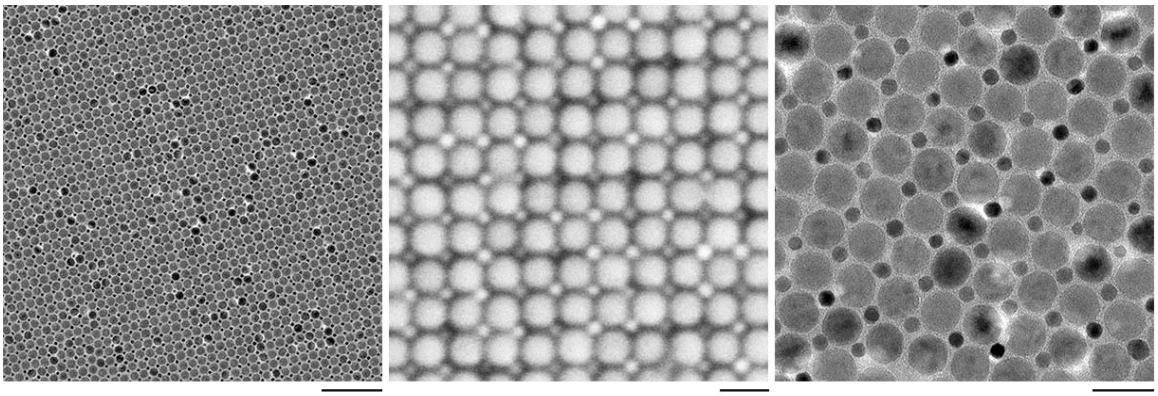

Fig. S3.

TEM and SEM images of a monolayer of an AB-type BNSL isostructural with the rock salt (NaCl) (*1*, *22*, *36*). The scale bars correspond to (L to R) 100 nm, 20 nm, and 20 nm. SEM images in our studies were acquired on an ULTRA 55 field-emission SEM or a SUPRA 55VP field emission SEM (both Carl Zeiss Microscopy, LLC), both operated at 5 kV.

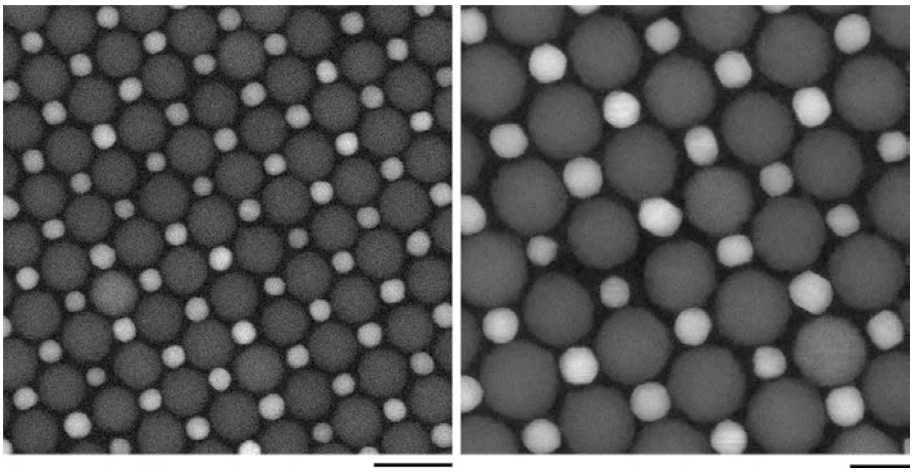

Fig. S4.

HAADF-STEM images of an AB-type BNSL. The scale bars correspond to 20 nm (left) and 10 nm (right). HAADF-STEM images in our studies were acquired on an aberration-corrected ‘cubed’ FEI-Titan electron microscope operated at 300 kV.

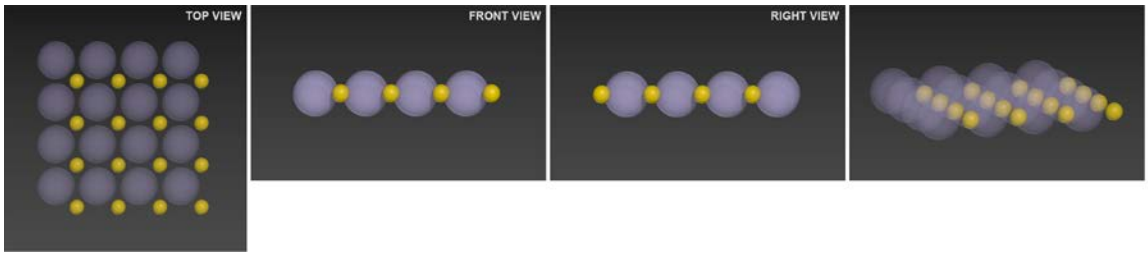

Fig. S5.

Structural model of the *vac*$_1$Au$_1$-type array. In this and the subsequent models, the filled yellow spheres represent Au NPs and the semi-transparent purple spheres represent vacancies corresponding to the positions of etched Fe_3O_4 NPs.

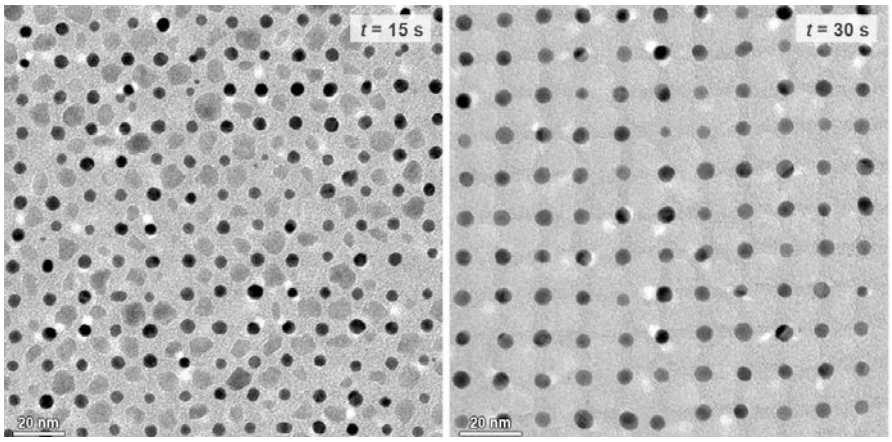

Fig. S6.

Following etching on carbon-coated nitrocellulose. Here, an AB-type BNSL was immersed into an aqueous HCl solution for 15 s (left) and 30 s (right).

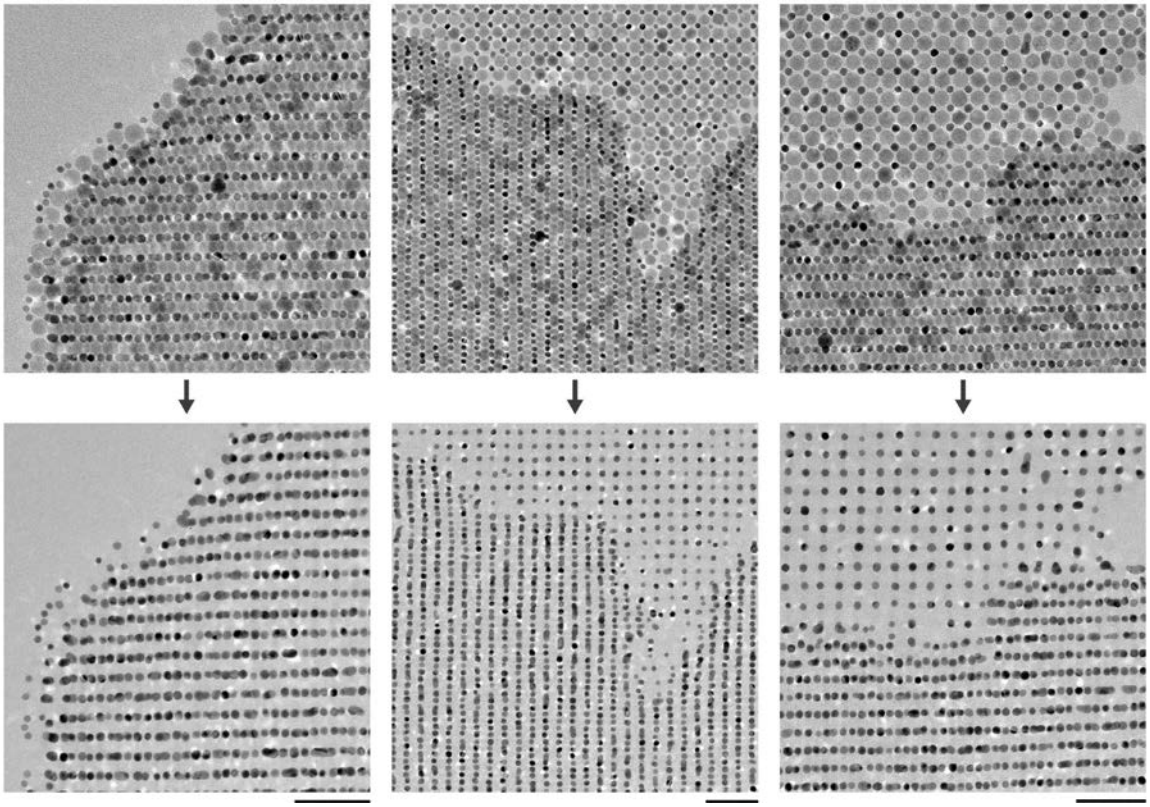

Fig. S7.

Additional examples of selective etching of Fe_3O_4 NPs with HCl without the disturbance of Au NPs. For clarity, we intentionally focused on the edge of the BNSL or regions containing defects. The scale bars correspond to 50 nm.

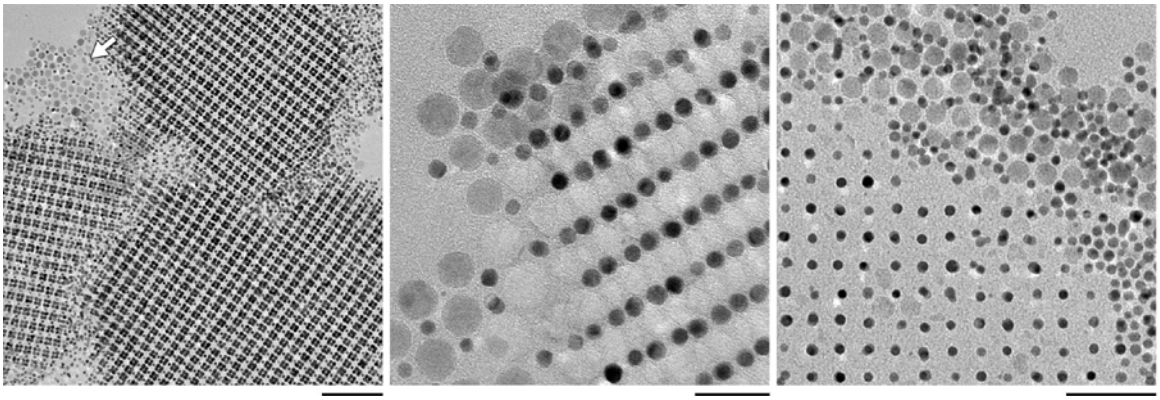

Fig. S8. Preferential etching of ordered arrays

The arrow in the image on the left points at unetched, disordered Fe_3O_4 NPs. In contrast, no residual Fe_3O_4 can be seen within ordered arrays. Preferential etching within ordered arrays can be explained by the particles having lost their protective organic coating. These observations suggest that regular arrangement of the NPs facilitates ligand desorption during mild thermal treatment. The scale bars correspond to (L to R) 100 nm, 20 nm, and 50 nm.

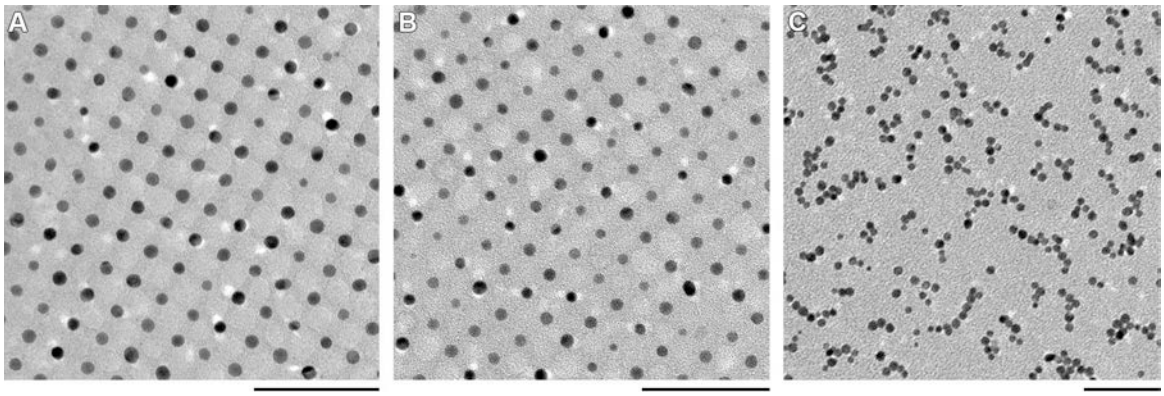

Fig. S9. Effect of the underlying substrate on the fixation of the NPs

An AB-type BNSL was deposited onto a homemade carbon-coated nitrocellulose film (left), a commercial carbon-coated Formvar film (center), and a nitrocellulose film lacking the carbon coating (right). Following thermal treatment under the same conditions, the BNSLs were treated with aqueous HCl. The scale bars correspond to 50 nm.

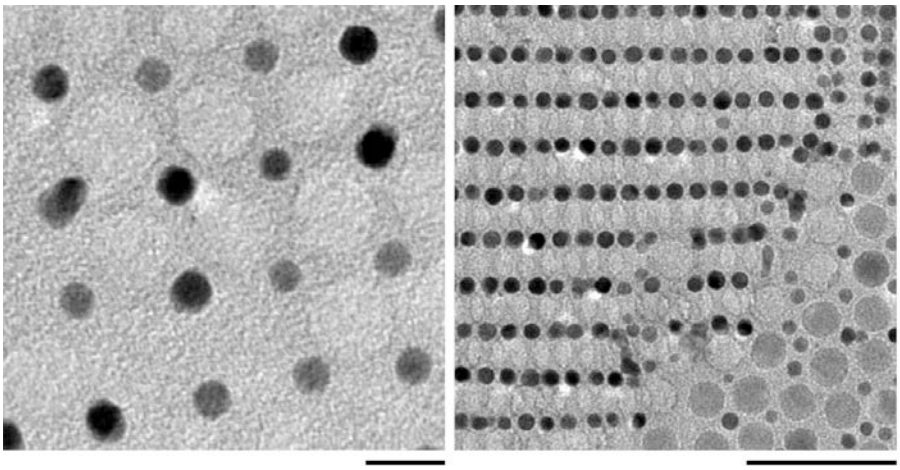

Fig. S10.

Residual carbonaceous films (seen in low contrast) observed after thermal treatment of AB-type BNSLs followed by etching with aqueous HCl. The films immobilize the Au NPs onto the underlying amorphous carbon film. The scale bars correspond to 10 nm (left) and 50 nm (right).

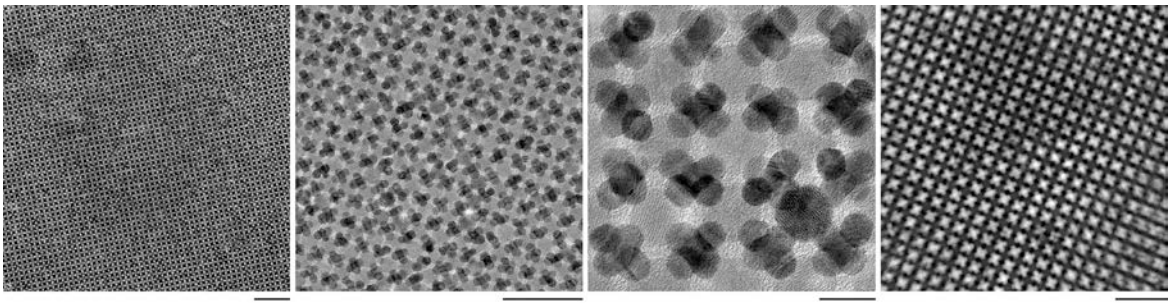

Fig. S11.

TEM images of an AB_6-type BNSL (lacking the top layer of Au NPs; the image on the right is a HAADF-STEM image taken using an FEI (Philips) Tecnai T12 operated at 120 kV). The scale bars correspond to (L to R) 100 nm, 50 nm, 10 nm, and 50 nm.

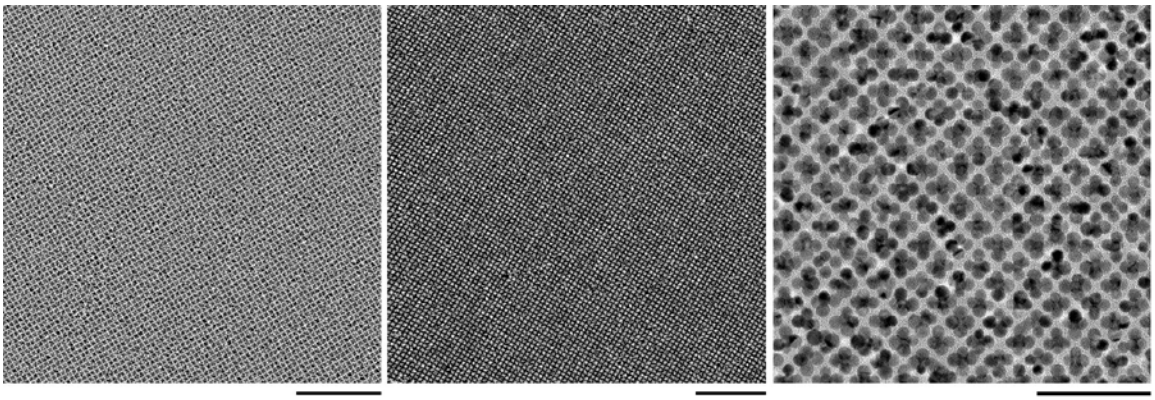

Fig. S12.

TEM images of a *vac*$_1$Au$_5$-type array. The scale bars correspond to (L to R) 200 nm, 200 nm, and 50 nm.

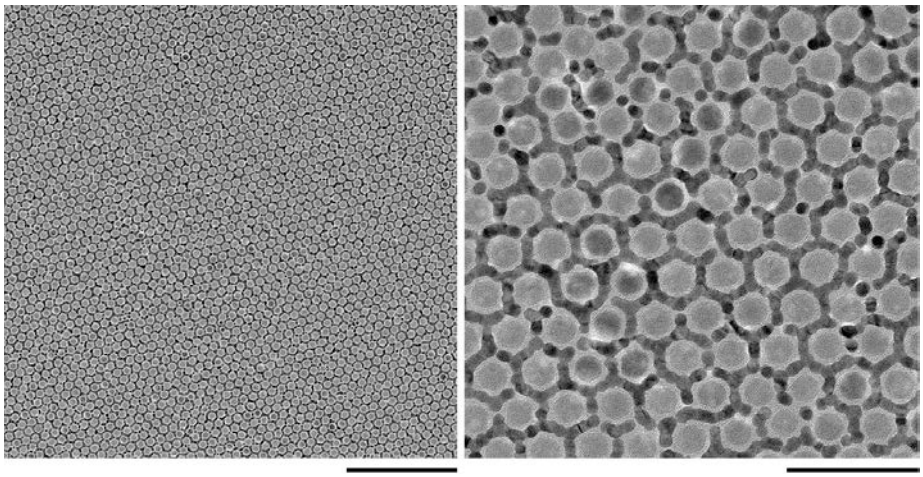

Fig. S13.

TEM images of a $CaCu_5$-type (*22*, *37*, *38*) BNSL (the [001] projection). This type of BNSL was occasionally found to coexist with the AB_6-type BNSL shown in Fig. 2A (see also fig. S15 below). The scale bars correspond to 200 nm (left) and 50 nm (right).

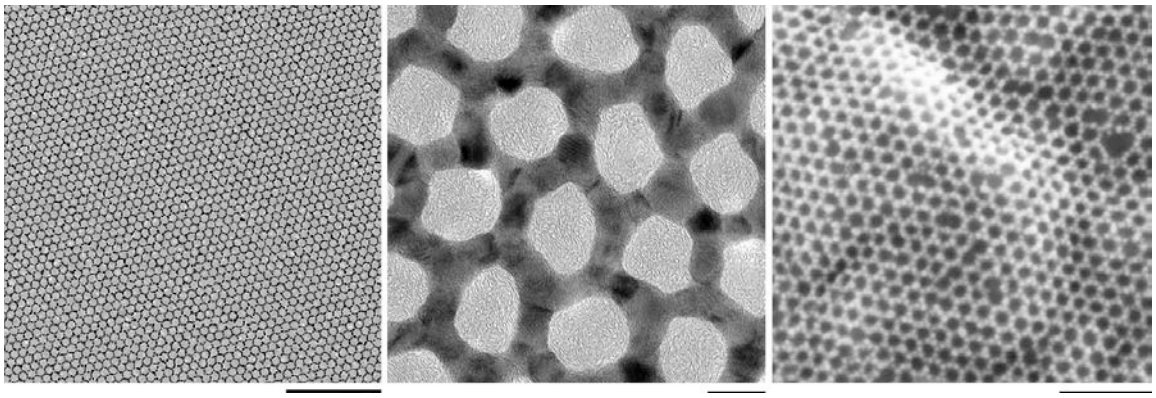

Fig. S14.

TEM (left, center) and SEM (right) images of honeycomb membranes obtained by thermal treatment and HCl etching of the $CaCu_5$-type BNSLs shown in fig. S13. The scale bars correspond to (L to R) 200 nm, 10 nm, and 100 nm.

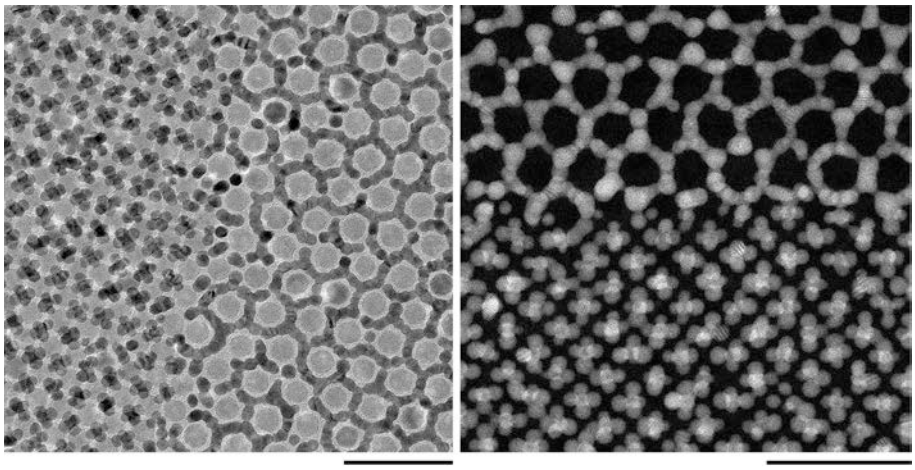

Fig. S15.

TEM (left) and HAADF-STEM (right) images showing an epitaxial relationship between the $CaCu_5$-type BNSL and the AB_6-type BNSL (shown in Fig. 2A). The STEM image was recorded after HCl etching. The scale bars correspond to 50 nm.

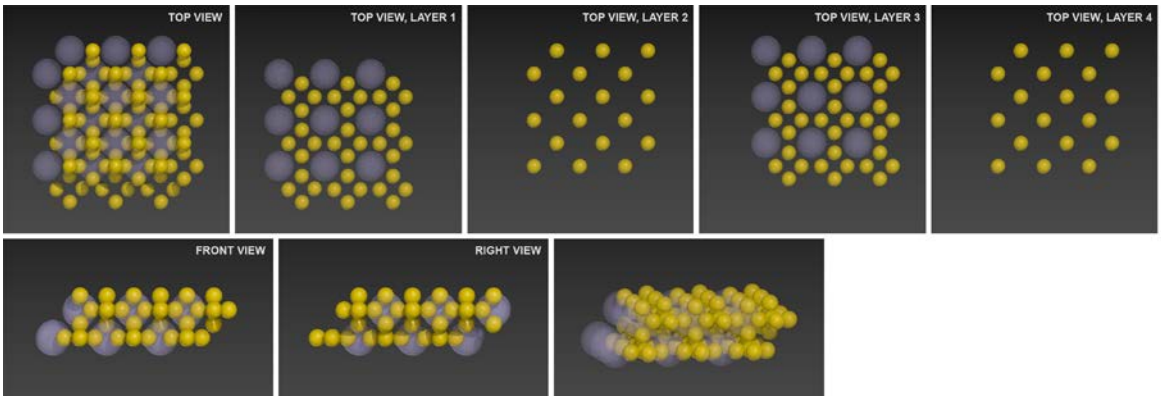

Fig. S16.
Structural model of the *vac*$_1$Au$_6$-type array.

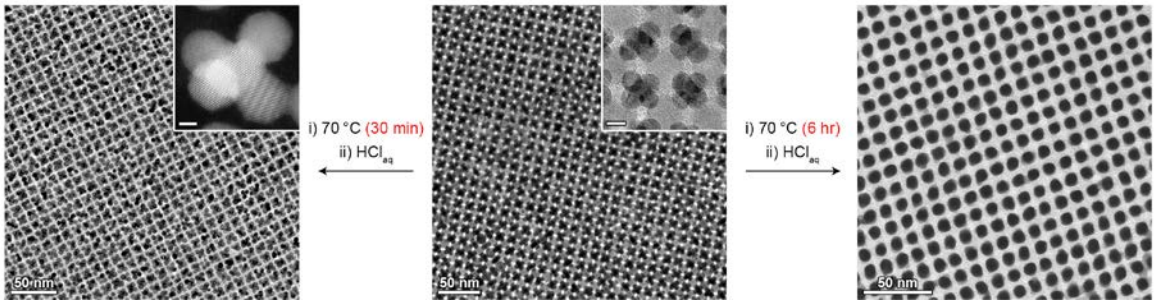

Fig. S17.

Effect of heating time on the morphology of the non-close-packed NP array obtained from the AB_6-type BNSL (here, lacking the top layer of Au NPs). The scale bars in the insets correspond to 5 nm (center) and 2 nm (left).

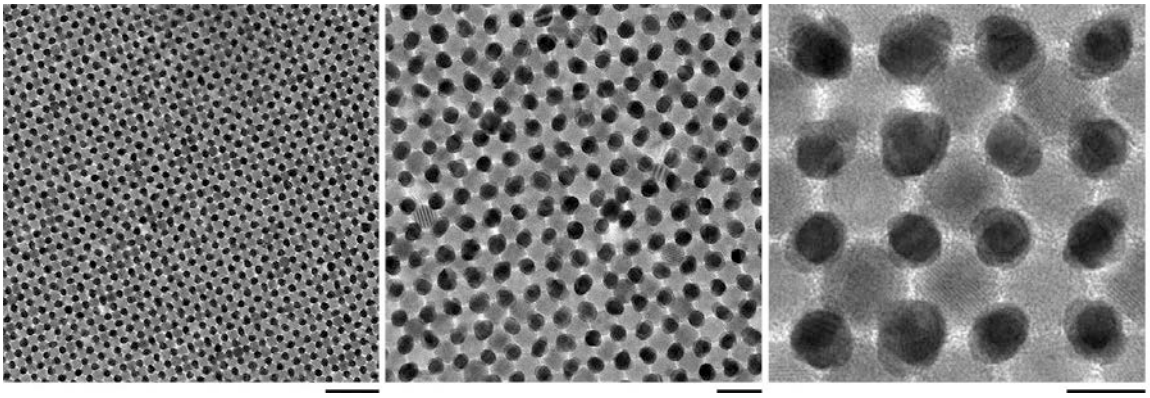

Fig. S18.

TEM images of an AB-type BNSL obtained by heating the AB_6-type BNSL (lacking the top layer of Au NPs) at 70 °C for 4 hours. The scale bars correspond to (L to R) 50 nm, 20 nm, and 10 nm.

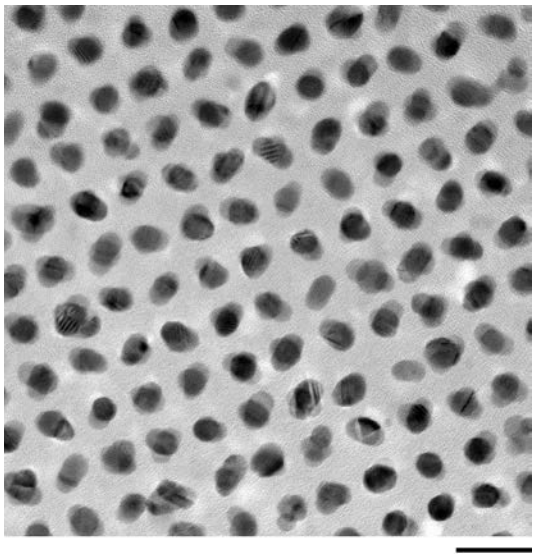

Fig. S19.

TEM image of an array of partially sintered clusters of Au NPs obtained by etching the BNSLs shown in fig. S18. The scale bar corresponds to 20 nm.

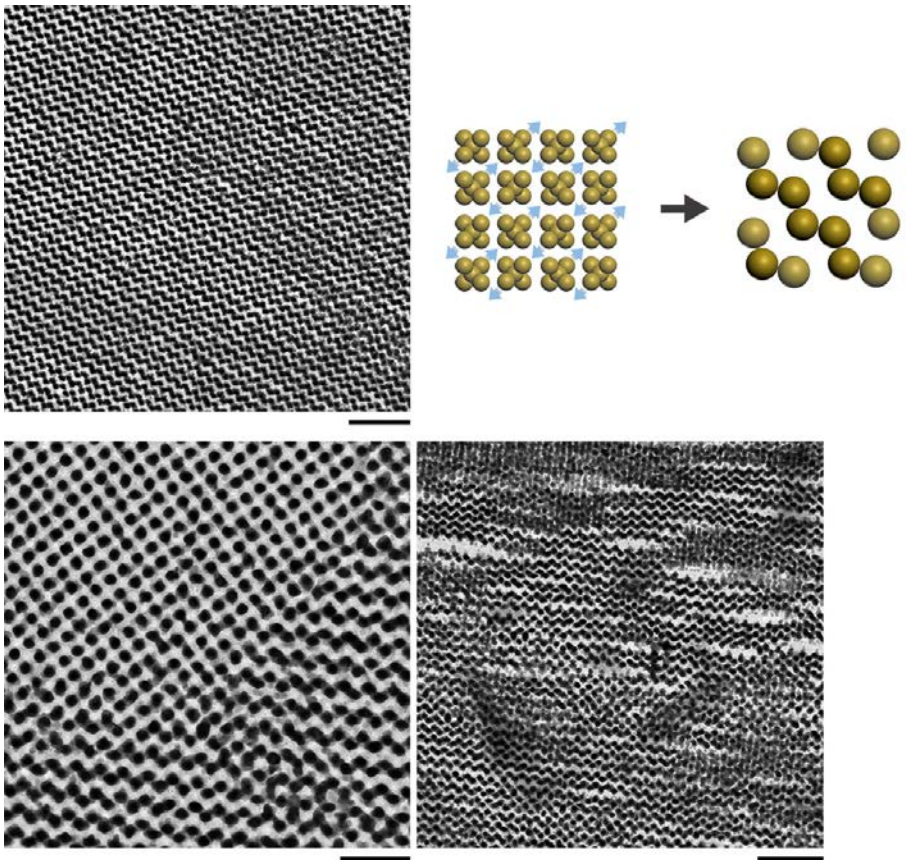

Fig. S20.

TEM images of zigzag-type nanowires obtained by simultaneous translation and coalescence of clusters of Au NPs as shown in the scheme in the top right (we found that this transformation was facilitated in the presence of oleic acid present in the system). The scale bars correspond to 100 nm (top), 50 nm (bottom left) and 100 nm (bottom right).

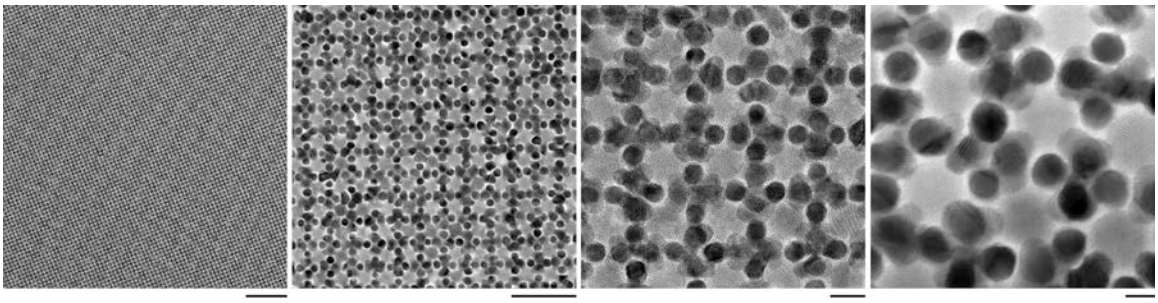

Fig. S21.

TEM images of an AB_{11}-type BNSL, where the top layer of Au NPs consists of Au quartets. The scale bars correspond to (L to R) 200 nm, 50 nm, 10 nm, and 5 nm.

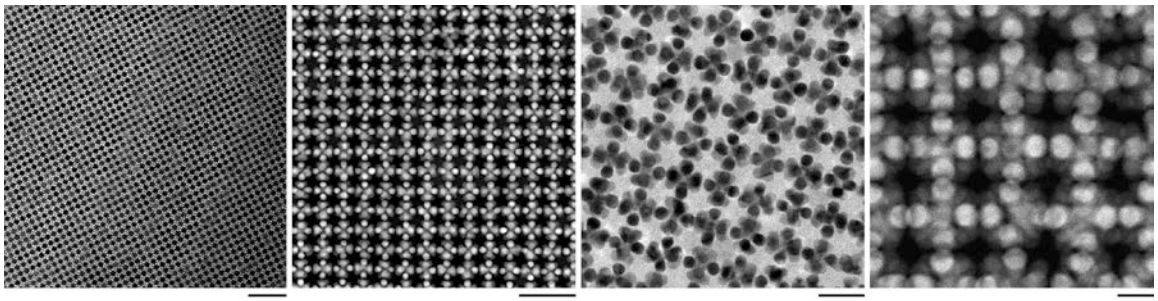

Fig. S22.

HAADF-STEM and TEM images of vac_1Au_{11}-type arrays, where the top layer consists of Au quartets. The scale bars correspond to (L to R) 100 nm, 50 nm, 20 nm, and 10 nm.

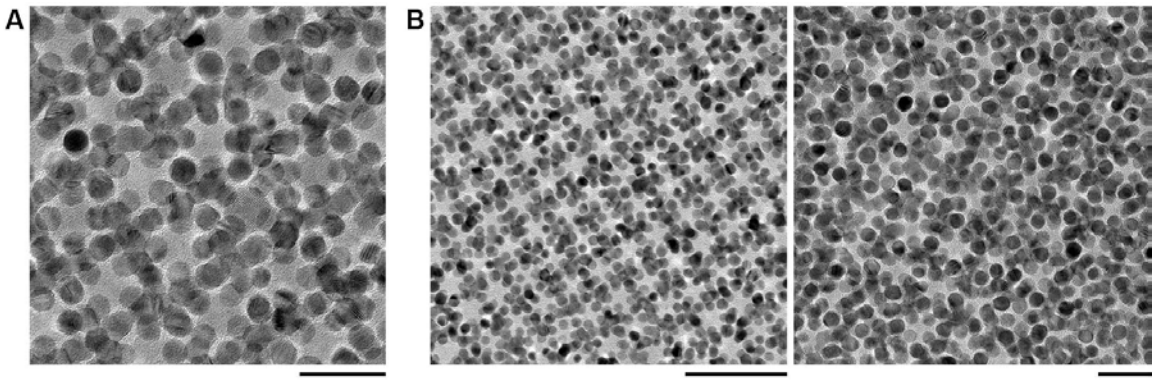

Fig. S23.

(**A**) TEM image of an AB_{11}-type BNSL containing NP septets in the top layer of Au NPs. (**B**) TEM images of the corresponding (post-etching) *vac*$_1$Au$_{11}$-type array. The scale bars correspond to 20 nm (A), 50 nm (B, *left*), and 20 nm (B, *right*).

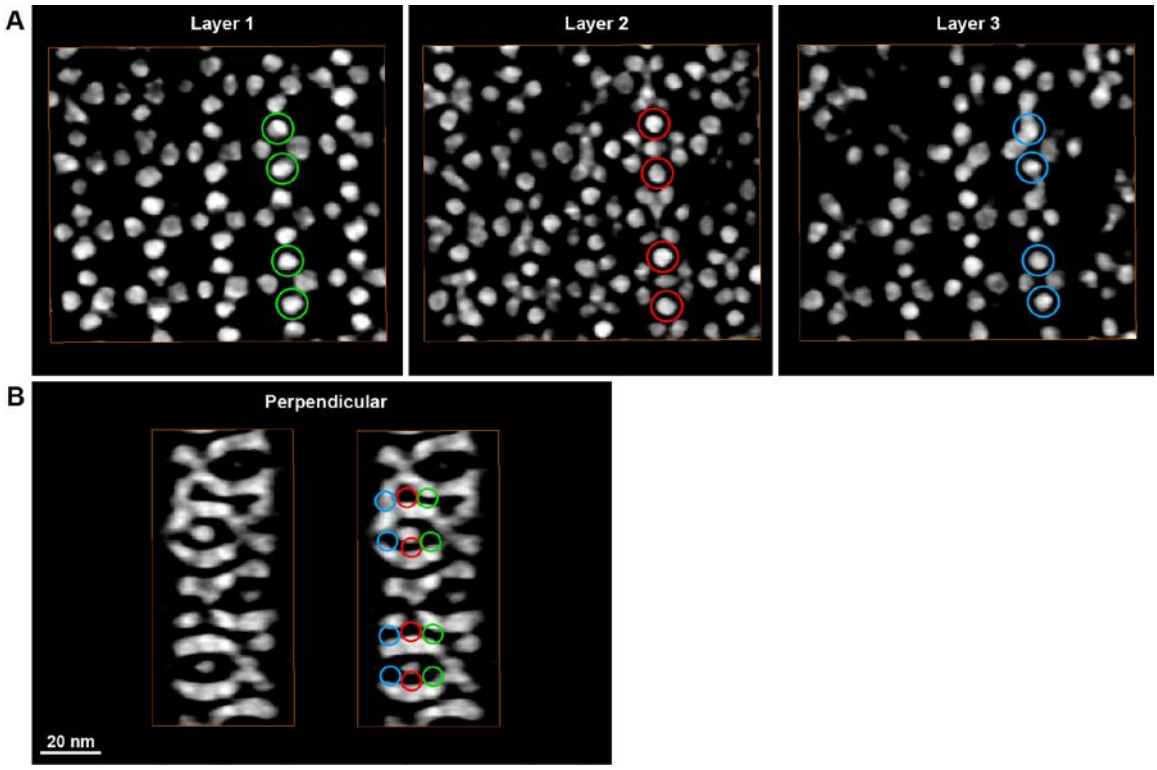

Fig. S24. Orthoslices through the reconstructed volume of the AB_{11} -type BNSL

(**A**) Orthoslices presenting the initial three layers of the structure. (**B**) Orthoslice through the reconstructed volume rotated 90° clockwise along the y-axis with respect to the orthoslices in the upper panel. The differently colored circles on the right correspond to the locations indicated in (A). As can be seen, a combination of missing wedge artifacts and sintering makes it difficult to resolve individual NPs along this direction. HAADF-STEM tomography series in our studies were acquired by using an aberration-corrected 'cubed' FEI-Titan electron microscope operated at 300 kV. Electron tomography series were acquired manually by using a Fischione model 2020 single-tilt tomography holder and reconstructed by using the simultaneous iterative reconstruction algorithm (SIRT) implemented in the ASTRA toolbox (*39*). For the SIRT reconstructions, 120 iterations were used.

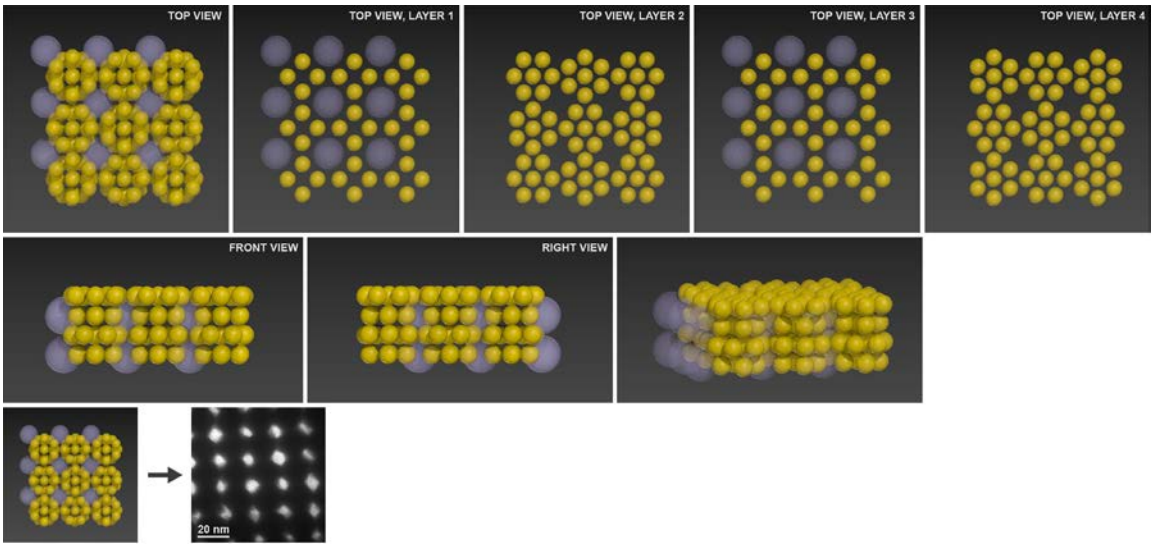

Fig. S25.

Structural model of the *vac*$_1$Au$_{11}$-type array. *Bottom*: Prolonged thermal treatment of the precursor BNSL results in partial sintering of Au NPs, resulting in the formation of a nanoporous membrane featuring regular arrays of nanopores (here, 7.0 ± 0.8 nm).

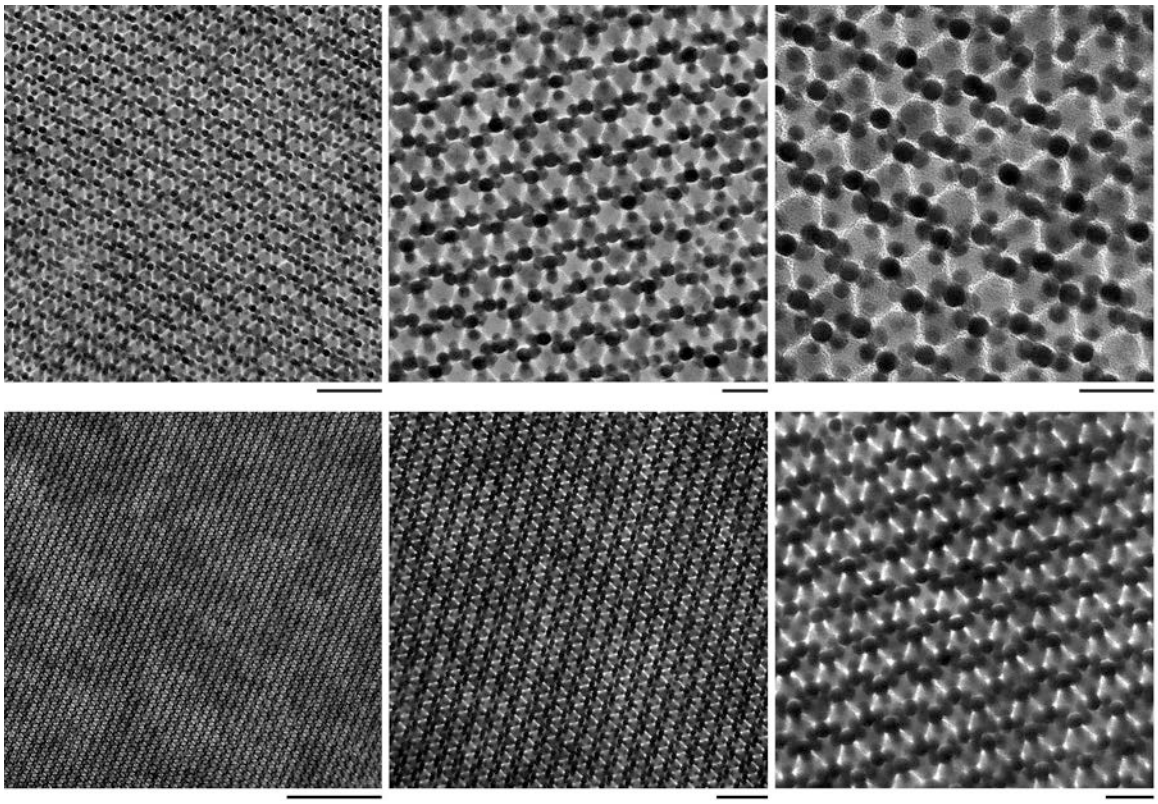

Fig. S26.

TEM images of AB_4-type BNSLs. The images in the top row correspond to monolayers of the AB_4 BNSL; the images in the bottom row are of thicker arrays. The scale bars correspond to (top row, L to R) 50 nm, 20 nm, and 20 nm, and (bottom row, L to R) 200 nm, 50 nm, and 20 nm.

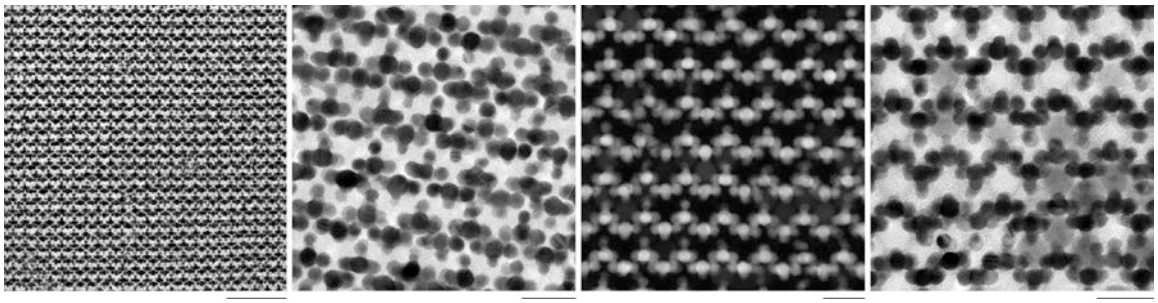

Fig. S27.

TEM and HAADF-STEM images of the *vac*$_1$Au$_1$Au′$_2$Au″$_1$-type array. The TEM image on the right was recorded before the complete etching of Fe_3O_4 NPs. The scale bars correspond to (L to R) 100 nm, 20 nm, 20 nm, and 20 nm.

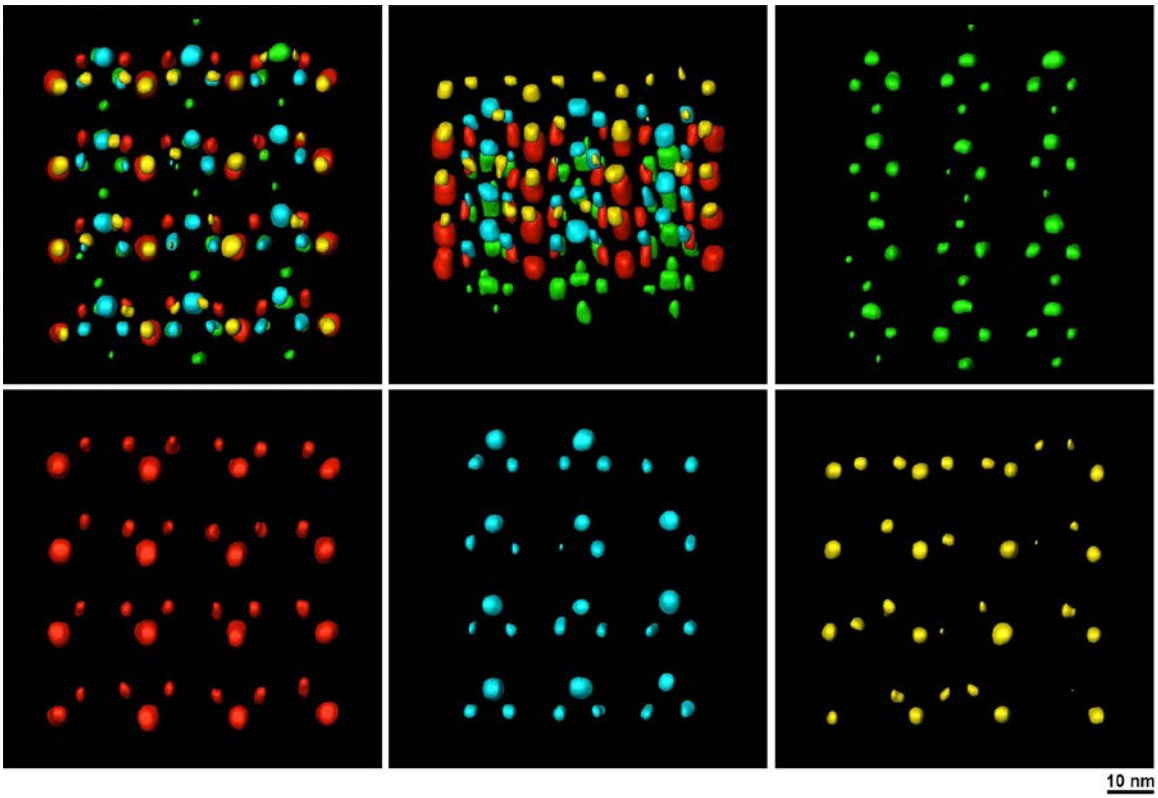

Fig. S28.

3D representations of a part of the reconstructed segmented volume of a *vac*$_1$Au$_1$Au′$_2$Au″$_1$-type array at different viewing directions. Note that the sample imaged here contained defects (some Au NPs are missing).

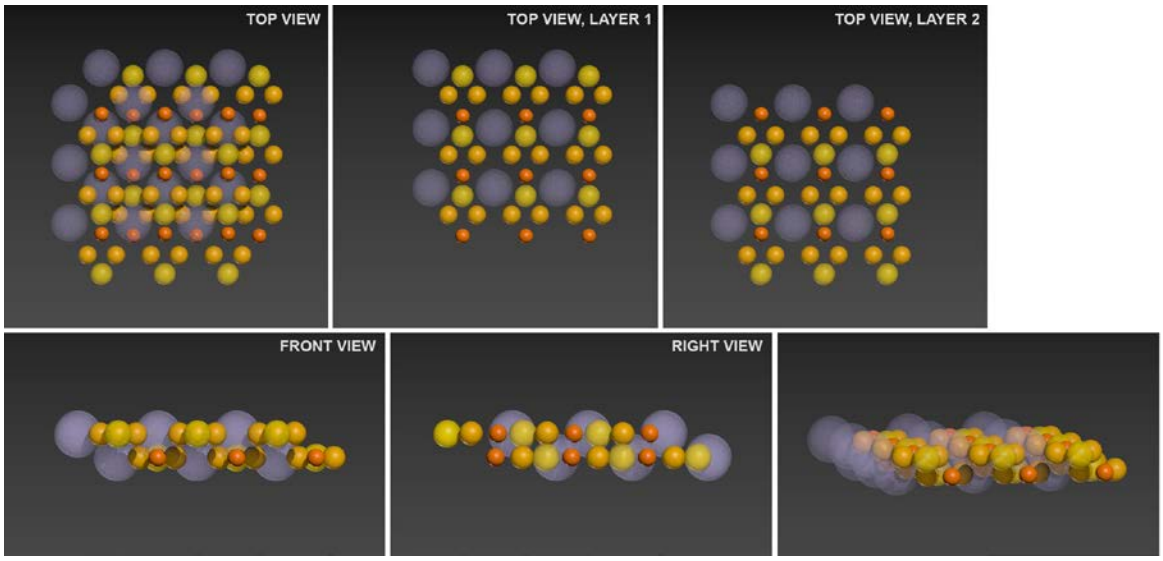

Fig. S29.

Structural model of the *vac*$_1$Au$_1$Au′$_2$Au″$_1$-type array. Gold NPs of three different sizes are shown in light yellow, dark yellow, and orange.

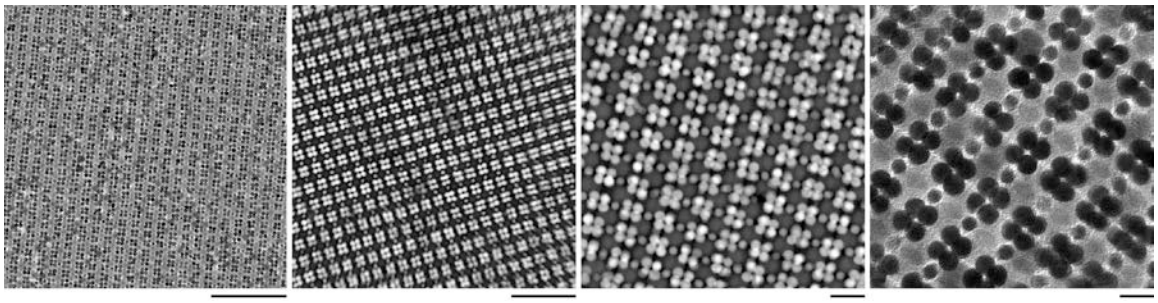

Fig. S30.

TEM and HAADF-STEM images of the ABC_4-type arrays. The scale bars correspond to (L to R) 100 nm, 50 nm, 20 nm, and 10 nm.

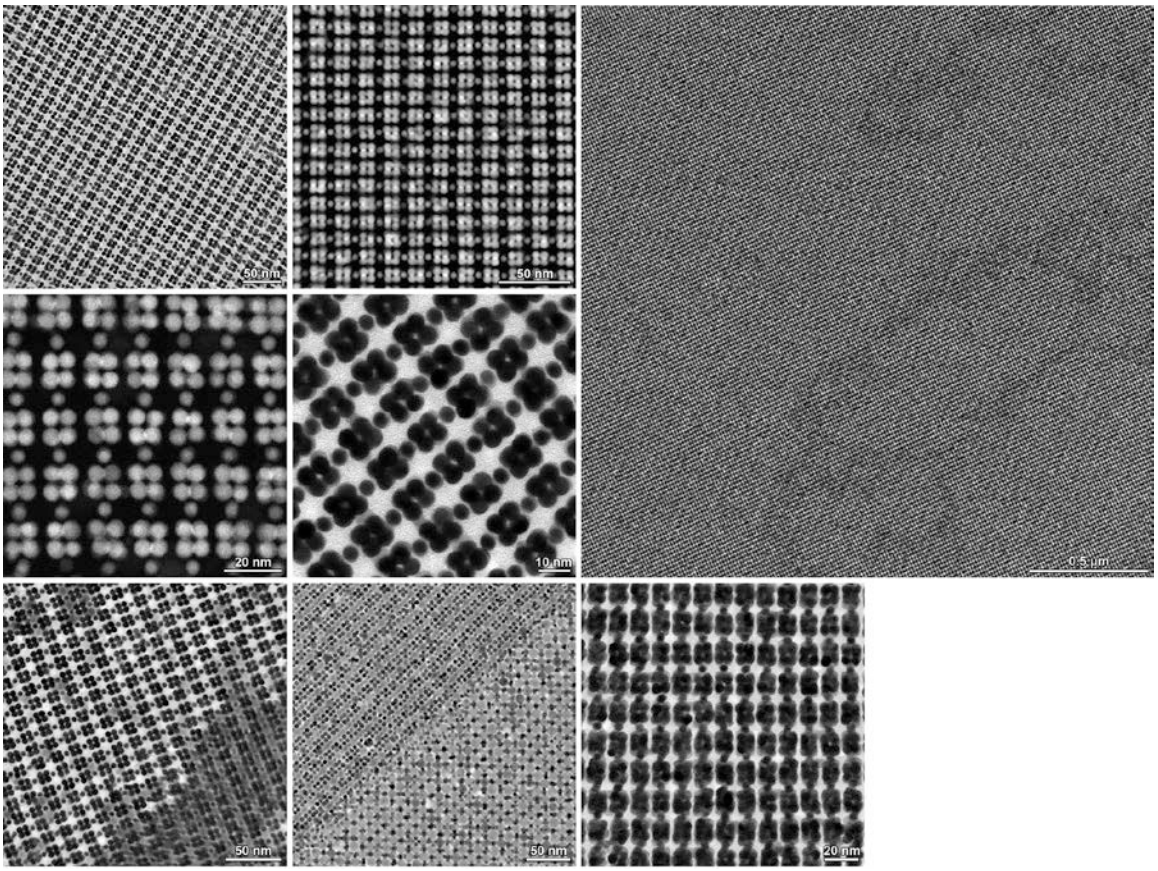

Fig. S31.

TEM and HAADF-STEM images of the *vac*$_1$Au$_4$Au′$_1$-type arrays. The TEM image in the bottom left was recorded before the complete etching of Fe_3O_4 NPs. The image next to it shows the coexistence of ABC_4- and AB_5-type BNSL. The expanded image in the top right shows an example of a large-scale, virtually defect-free array of *vac*$_1$Au$_4$Au′$_1$. The image in the bottom right shows a multilayer of the *vac*$_1$Au$_4$Au′$_1$-type array.

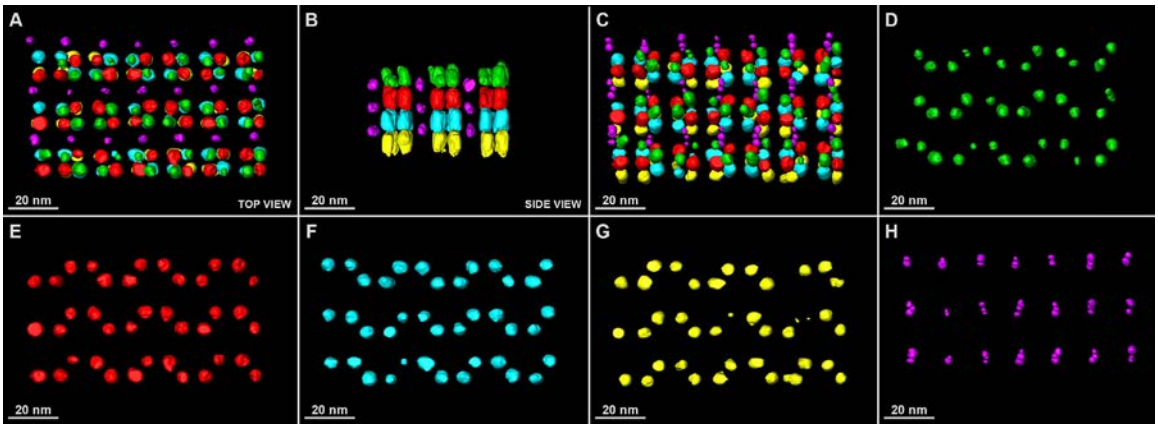

Fig. S32.

3D representations of a part of the reconstructed segmented volume of the $vac_1Au_1Au'_4$-type array at different viewing directions. In B, the volume is rotated 90° along the *y*-axis. In C, the structure is tilted by 8-10° along the *z*-axis. The images in D-G are views from the top; in H, the structure viewed from the top has been slightly rotated to highlight the presence of multiple layers. The different colors correspond to different segments along the *z*-axis.

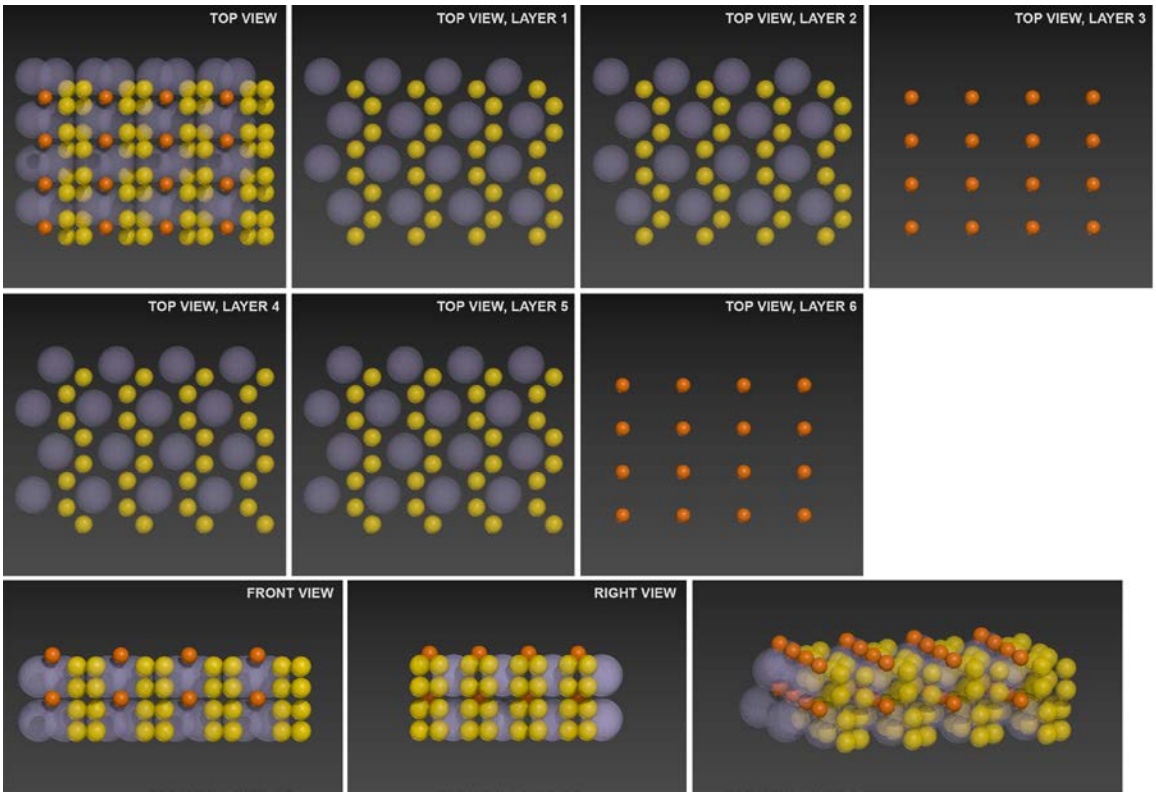

Fig. S33.

Structural model of the *vac*$_1$Au$_4$Au′$_1$-type array. Gold NPs of two different sizes are shown in yellow and orange.

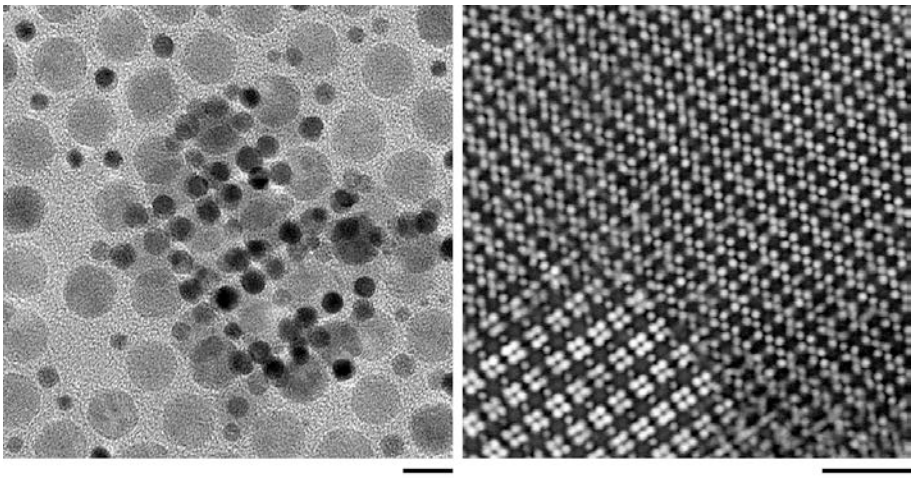

Fig. S34. Insights into the high stability of the ABC_4-type BNSL

Left: TEM image of a very small domain of the ABC_4-type BNSL. Notably, the domain is at least four Au NP-high (i.e., tetralayer), despite being surrounded by a sub-monolayer of NPs. *Right*: HAADF-STEM image showing a grain boundary between a $vac_1Au_1Au'_4$ and a vac_1Au_4 non-close-packed NP array (obtained by etching ABC_4-type and AB_4-type BNSLs, respectively) (note the epitaxial relationship) (in our experiments, we observed the coexistence of these two types of structures only once). The fact that the $vac_1Au_1Au'_4$ array in the bottom left of the HAADF-STEM image appears much brighter indicates that it is composed on a larger number of vertically stacked Au NPs. The scale bars correspond to 10 nm (L) and 50 nm (R).

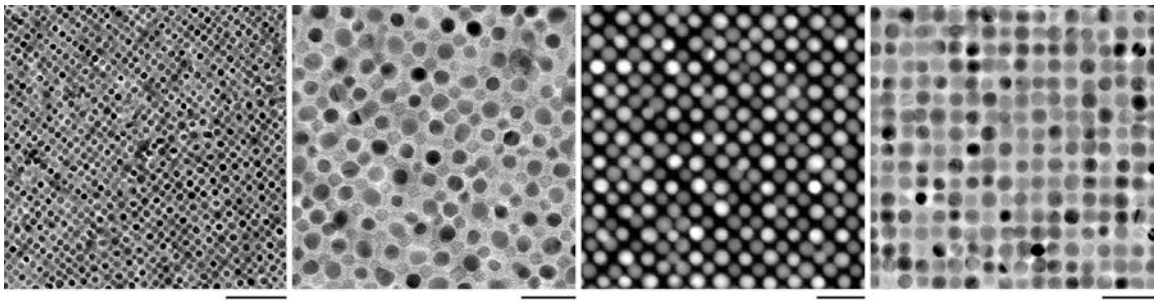

Fig. S35.

TEM and HAADF-STEM images of the "type I" bilayer of the *vac*$_1$Au$_1$-type array. The scale bars correspond to (L to R) 50 nm, 20 nm, 20 nm, and 20 nm.

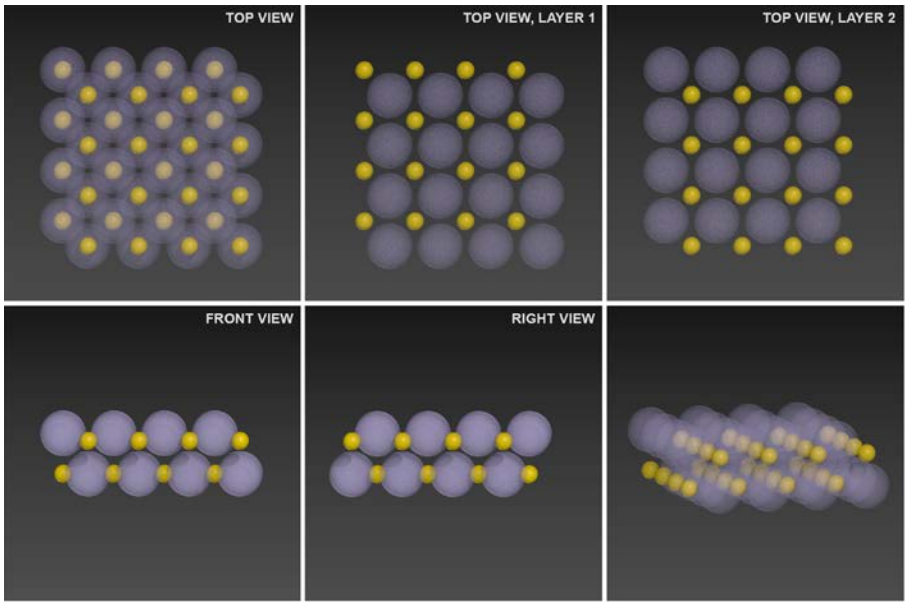

Fig. S36.
Structural model of the "type I" bilayer of the *vac*$_1$Au$_1$-type array.

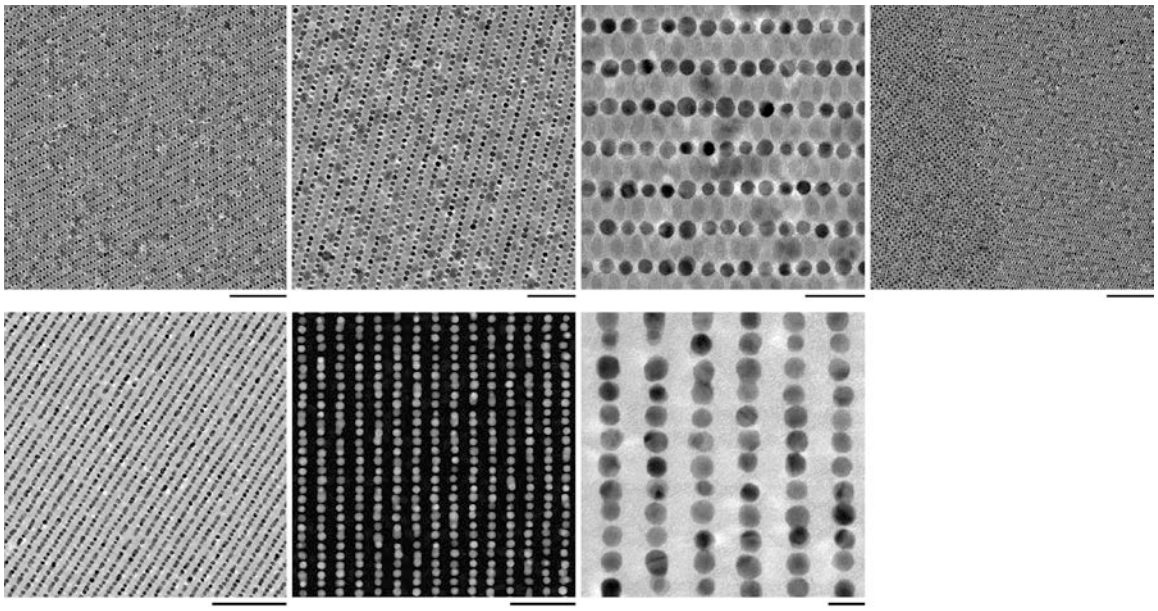

Fig. S37.

Top: TEM images of the “type II” bilayer of the AB-/NaCl-type BNSL. The scale bars correspond to (L to R) 100 nm, 50 nm, 20 nm, and 200 nm. *Bottom*: TEM and HAADF-STEM images of a bilayer of the *vac*$_1$Au$_1$-type array, where the two layers are stacked differently than in the samples shown in fig. S35. The scale bars correspond to (L to R) 100 nm, 50 nm, and 10 nm.

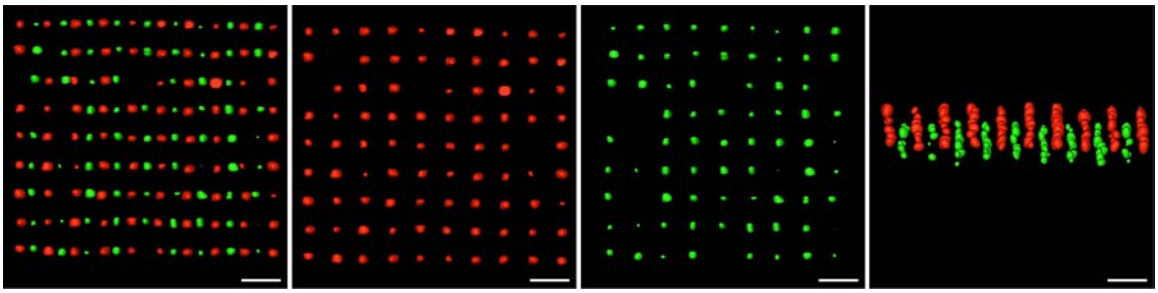

Fig. S38.

3D representations of a part of the reconstructed segmented volume of the “type II” bilayer of the *vac*$_1$Au$_1$-type array at different viewing directions. The scale bars correspond to 20 nm.

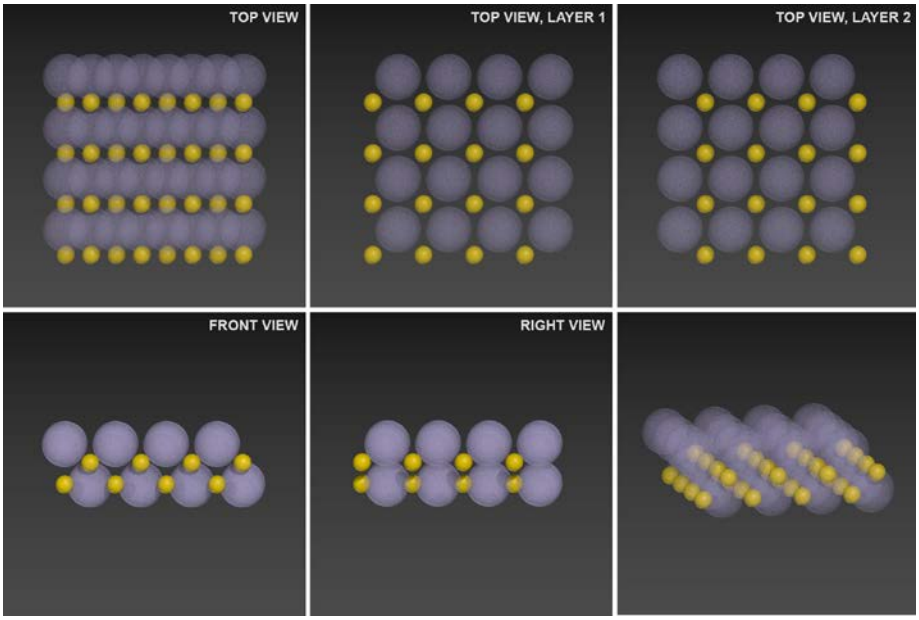

Fig. S39.
Structural model of the “type II” bilayer of the vac_1Au_1-type array.

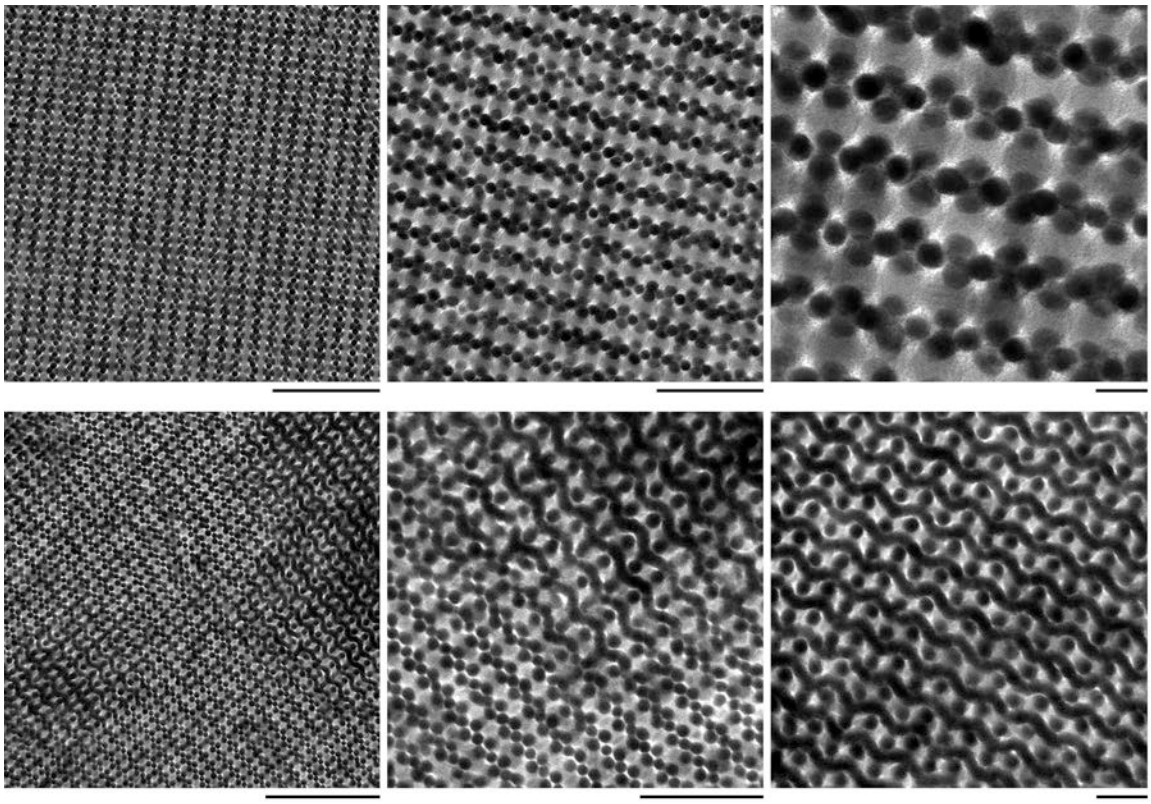

Fig. S40.

Top: TEM images of an AB_4-type BNSLs. The scale bars correspond to (L to R) 100 nm, 50 nm, and 10 nm. *Bottom*: TEM images of an AB_4-type BNSLs having undergone partial (center) or complete transformation into another type of AB_4-type BNSL. The scale bars correspond to (L to R) 100 nm, 50 nm, and 20 nm.

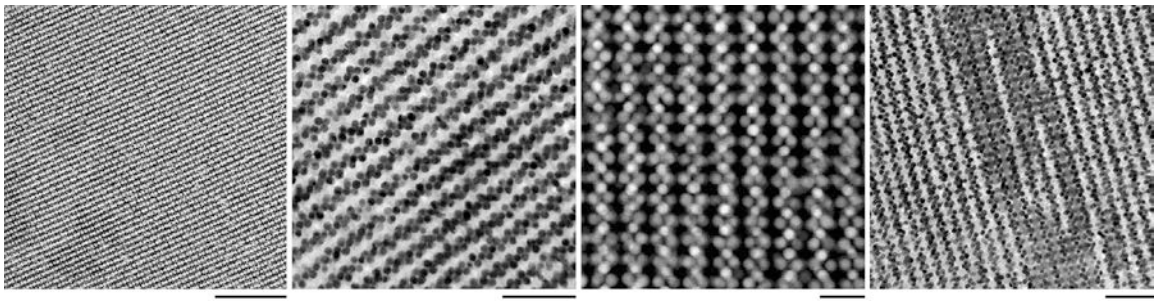

Fig. S41.

TEM and HAADF-STEM images of the *vac*$_1$Au$_4$-type array. Note that the image on the right was recorded before a complete etching of the Fe_3O_4 NPs. The scale bars correspond to (L to R) 200 nm, 50 nm, 20 nm, and 50 nm.

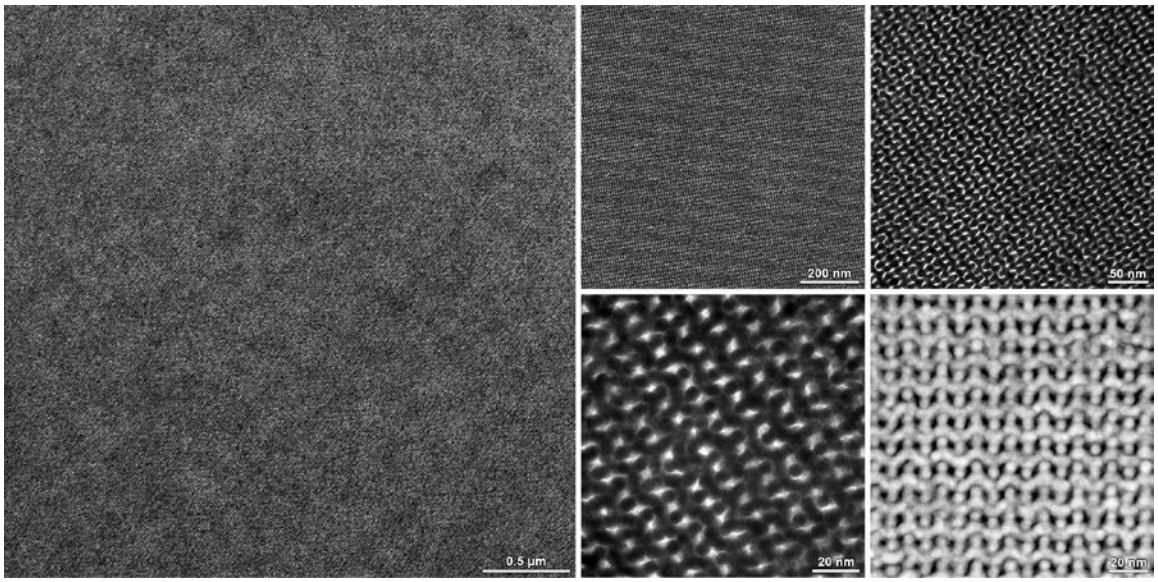

Fig. S42.
TEM and HAADF-STEM images of the *vac*$_1$Au$_4$-type array.

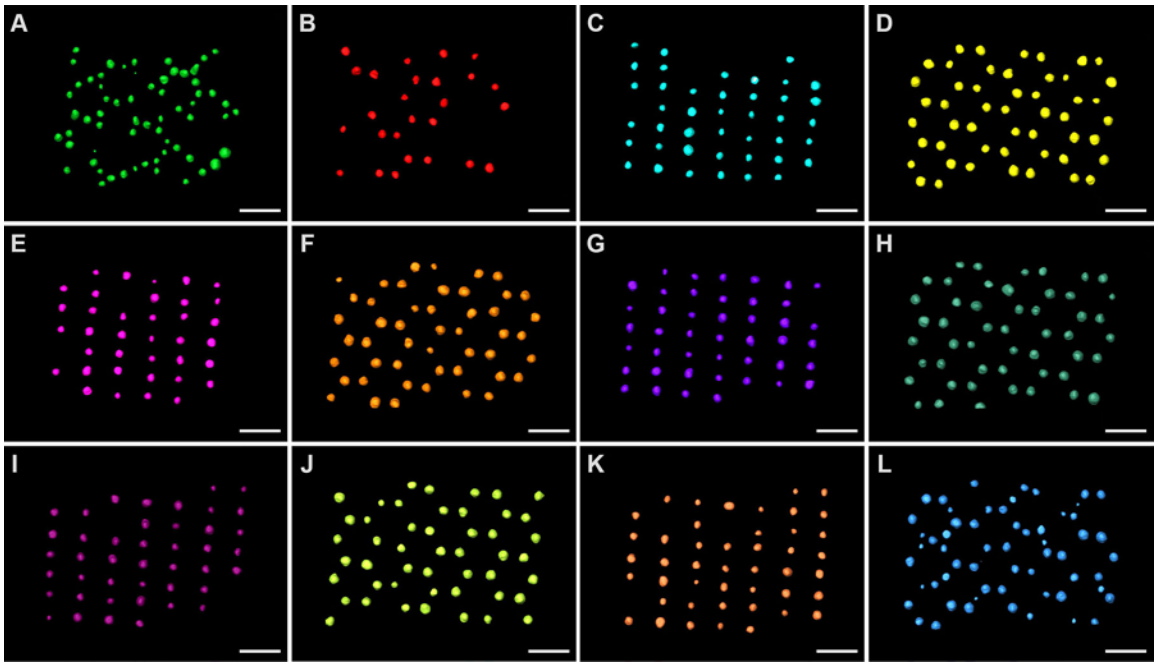

Fig. S43.

Different layers of the *vac*$_1$Au$_4$-type array shown in Fig. 3C. The scale bars correspond to 20 nm.

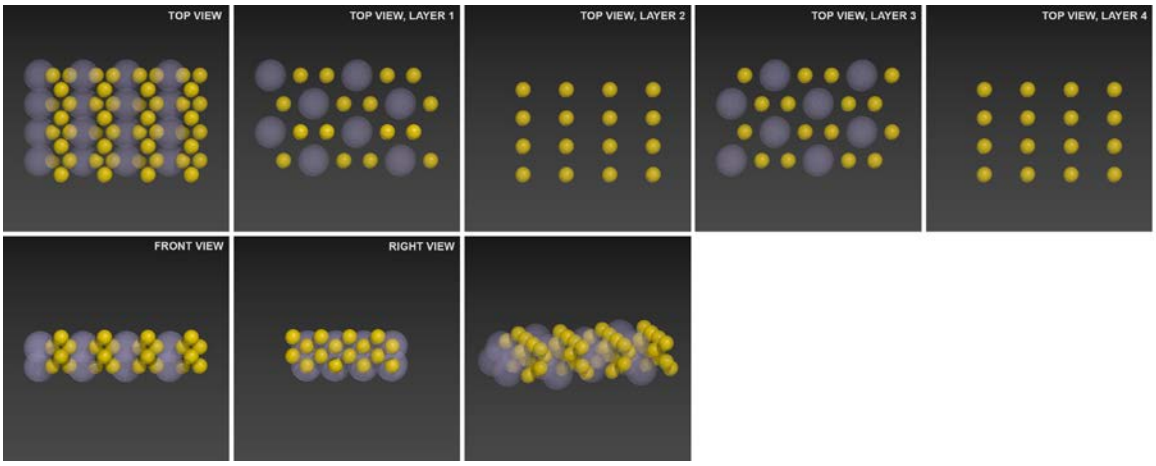

Fig. S44.
Structural model of the *vac*$_1$Au$_4$-type array.

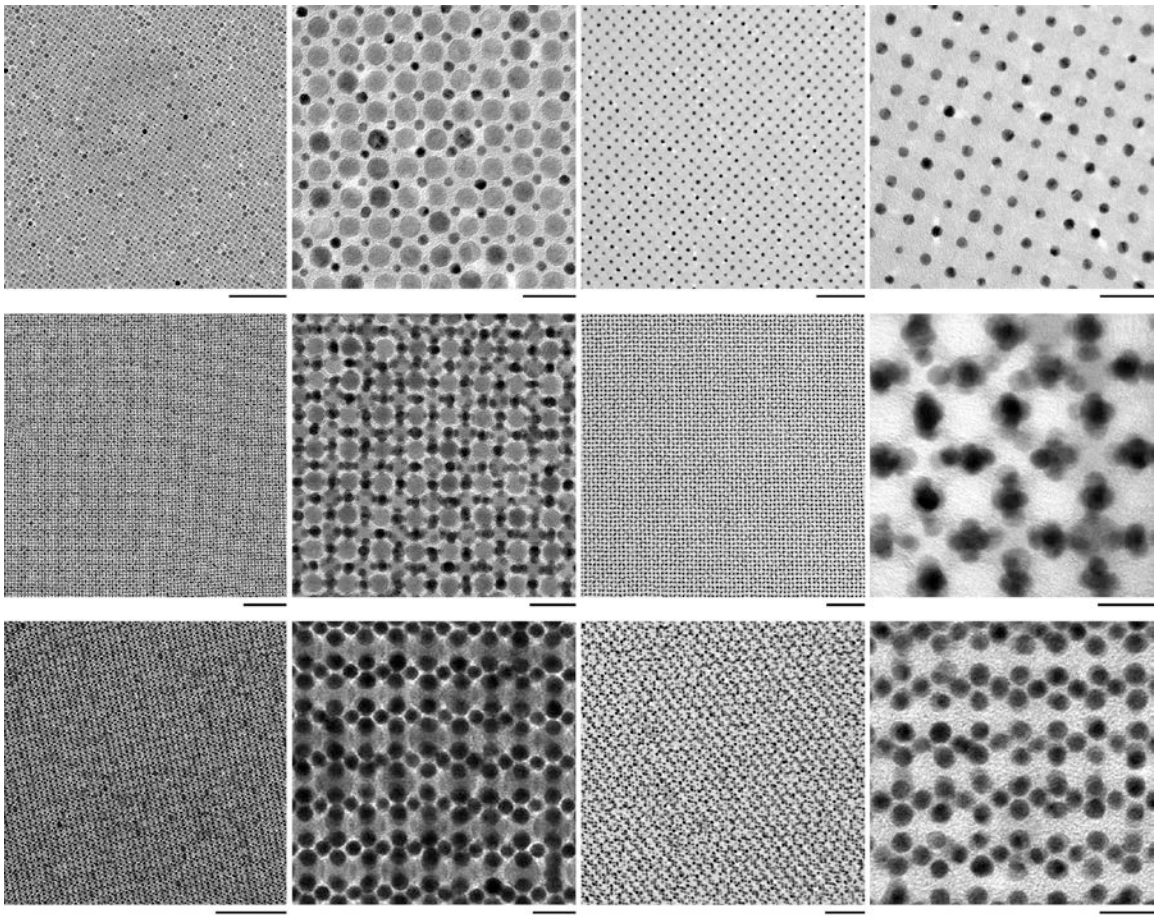

Fig. S45.

TEM images of binary superlattices co-assembled from 8.4 nm Fe_3O_4 NPs + 3.0 nm Au NPs and the resulting non-close-packed arrays. *Top row*: An AB-type BNSL and the corresponding *vac*$_1$Au$_1$-type array. The scale bars correspond to (L to R) 100 nm, 20 nm, 50 nm, and 20 nm. *Middle row*: An AB$_6$-type BNSL (without the top layer of Au NPs) and the corresponding *vac*$_1$Au$_5$-type array. The scale bars correspond to (L to R) 100 nm, 20 nm, 100 nm, and 10 nm. *Bottom row*: An AB$_4$-type BNSL and the corresponding *vac*$_1$Au$_4$-type array. The scale bars correspond to (L to R) 100 nm, 10 nm, 50 nm, and 10 nm.

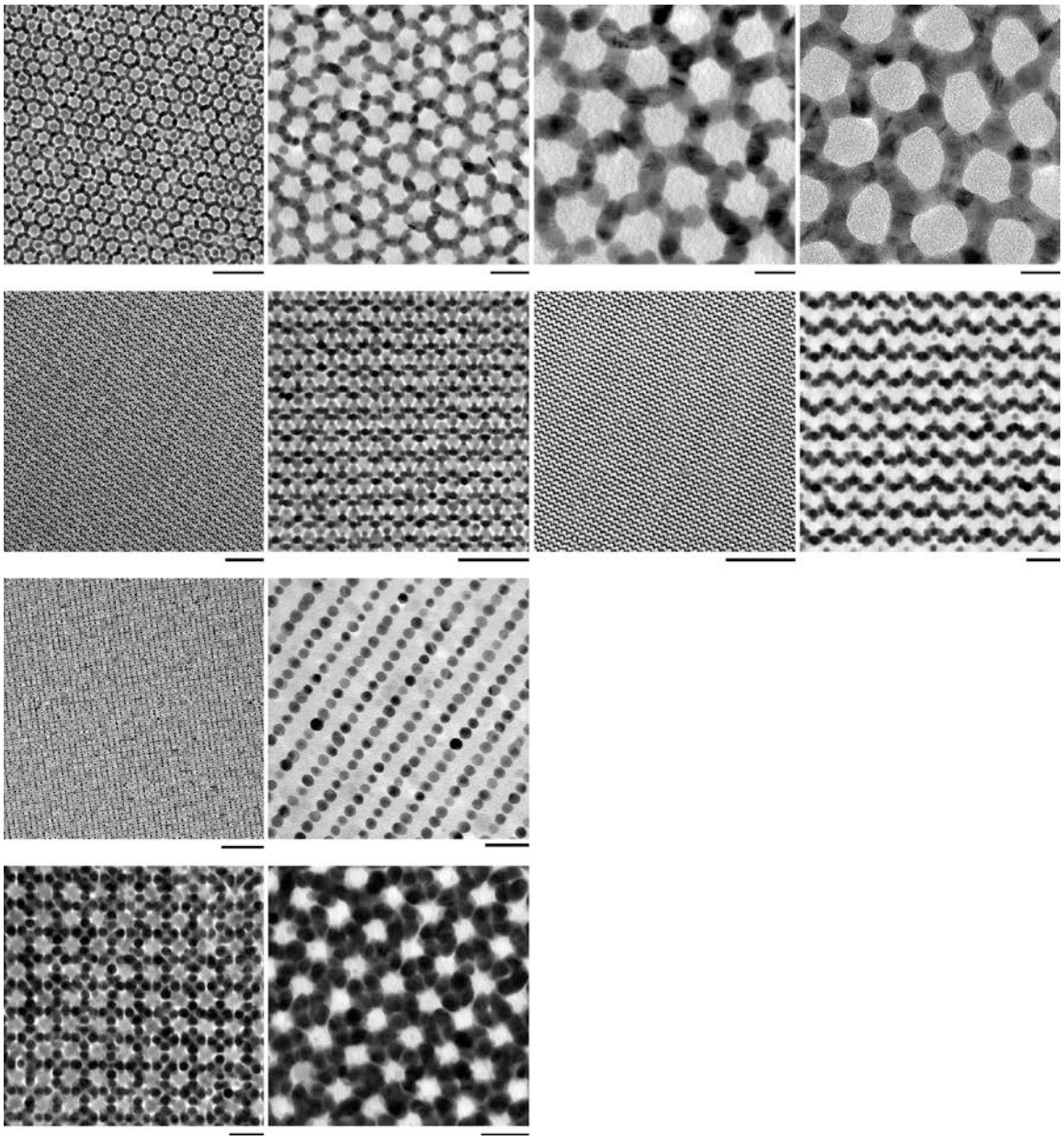

Fig. S46.

TEM images of binary superlattices co-assembled from 8.4 nm Fe_3O_4 NPs + 5.2 nm Au NPs and the resulting non-close-packed arrays. *First row* (L to R): An AB_5/$CaCu_5$-type BNSL; a *vac*$_1$Au$_5$-type array; a honeycomb membrane obtained by prolonged thermal treatment of the corresponding BNSL prior to etching; a honeycomb membrane obtained from a mixture of 10.6 nm Fe_3O_4 NPs and 5.2 nm Au NPs (taken from fig. S14 for comparison). The scale bars correspond to (L to R) 50 nm, 20 nm, 10 nm, and 10 nm. *Second row*: An AB_4-type BNSL and the corresponding *vac*$_1$Au$_1$Au$_2$′Au″$_1$-type array. The scale bars correspond to 100 nm, 50 nm, 200 nm, and 20 nm. *Third row*: A bilayer of an AB-type BNSL and the corresponding *vac*$_1$Au$_1$-type array. The scale bars correspond to 100 nm (*left*) and 20 nm (*right*). Fourth row: An AB_{11}-type BNSL and the corresponding *vac*$_1$Au$_{11}$-type array. The scale bars correspond to 20 nm.

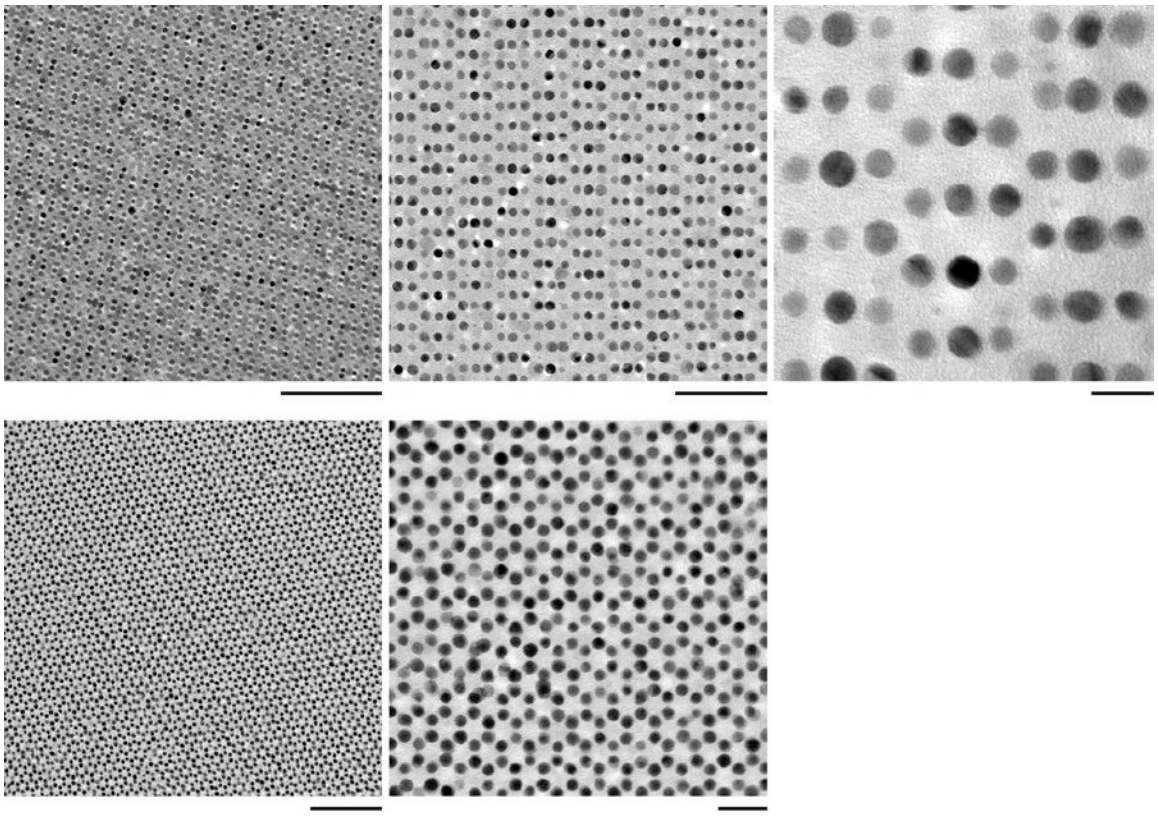

Fig. S47.

TEM images of additional binary superlattices obtained by co-assembly of 8.4 nm Fe_3O_4 NPs + 5.2 nm Au NPs and the resulting non-close-packed arrays. *Top*: An A_5B_3-type BNSL and the corresponding *vac*$_5$Au$_3$-type array. The scale bars correspond to (L to R) 100 nm, 50 nm, and 10 nm. *Bottom*: An AB_2-type BNSL and the corresponding *vac*$_1$Au$_2$-type array. The scale bars correspond to 100 nm (*left*) and 20 nm (*right*).

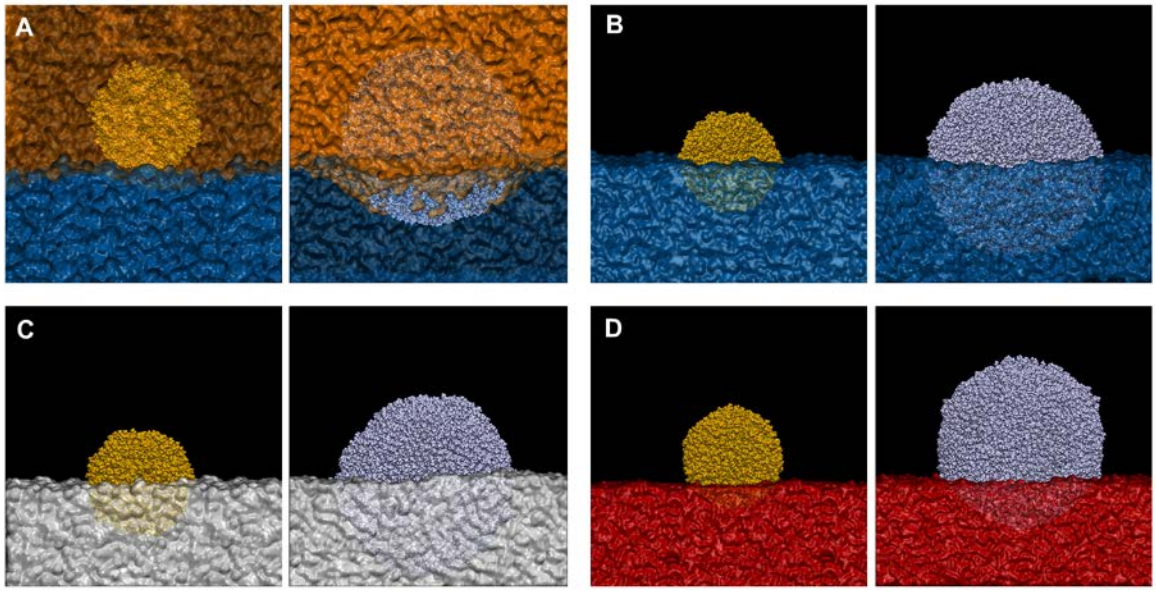

Fig. S48.

Individual Au NPs (on the left of each panel) and Fe_3O_4 NPs (on the right) relaxed at different interfaces: (**A**) DEG-hexane interface; (**B**) DEG-vacuum interface; (**C**) EG-vacuum interface; (**D**) water-vacuum interface. DEG, hexane, water, and EG are shown in dark blue, orange, dark, red, and light gray, respectively. Au NPs and Fe_3O_4 NPs are shown in yellow and light purple, respectively. Transparency levels of orange and blue surfaces in panel **A** are modulated for clarity so that Au NP is visible when immersed fully in hexane, and hexane is visible when Fe_3O_4 NP is almost fully immersed in hexane during the course of simulations.

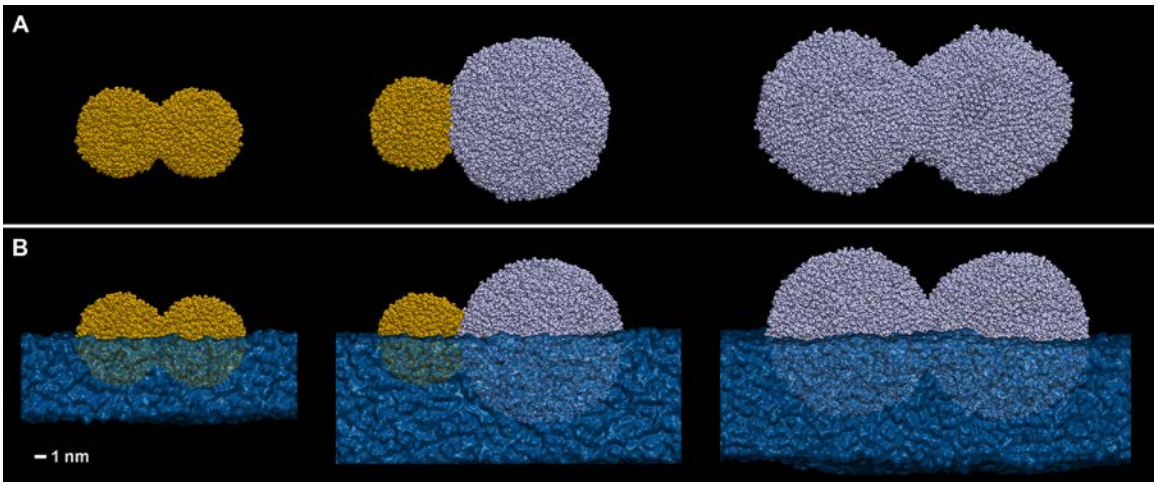

Fig. S49.

Nanoparticle pairs in vacuum (**A**) and at the DEG-vacuum interface (**B**) after 40 ns and 32 ns of simulations, respectively. From the left to the right: a pair of Au NPs; a pair of Au NP and Fe_3O_4 NP; a pair of Fe_3O_4 NPs. Au NPs are shown in yellow and Fe_3O_4 NPs in light purple. DEG is shown in dark blue.

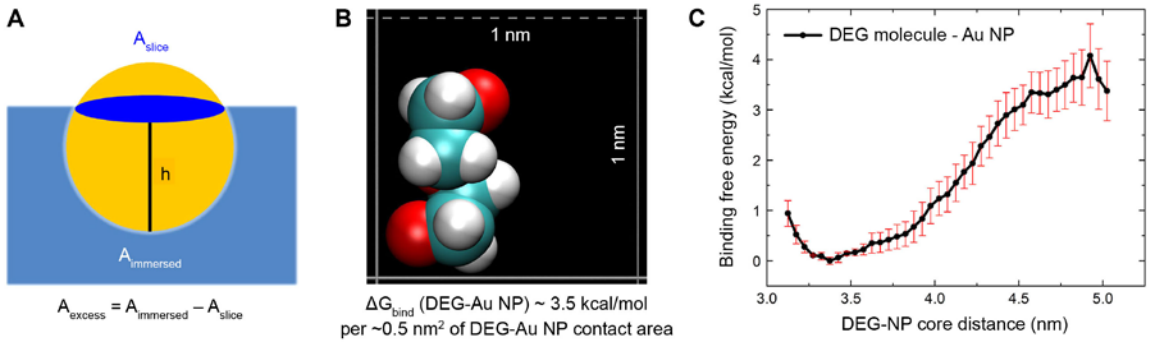

Fig. S50.

Estimating energy change upon immersing a dodacenethiol-functionalized Au NP from the DEG-vacuum interface into DEG. (**A**) Scheme of a partially immersed NP. Surface area of the immersed NP can be calculated as the surface area of the spherical cap without the base, $A_{immersed} = 2\pi Rh$, where R is the radius of the ligand-functionalized gold NP estimated as ~3.5 nm, and h is the immersion height defined in the scheme. The surface area of the slice shown (i.e., the surface area of the solvent prior to NP immersion) can be calculated as the area of the base of the spherical cap, $A_{slice} = \pi(2Rh–h^2)$. (**B**) The size of a single DEG molecule; the contact area between the DEG molecule and a gold NP surface is estimated as ~0.5 nm^2. (**C**) Free energy of binding between a single DEG molecule and a gold NP in vacuum, determined in umbrella sampling calculations. See also Fig. 2L in the main text.

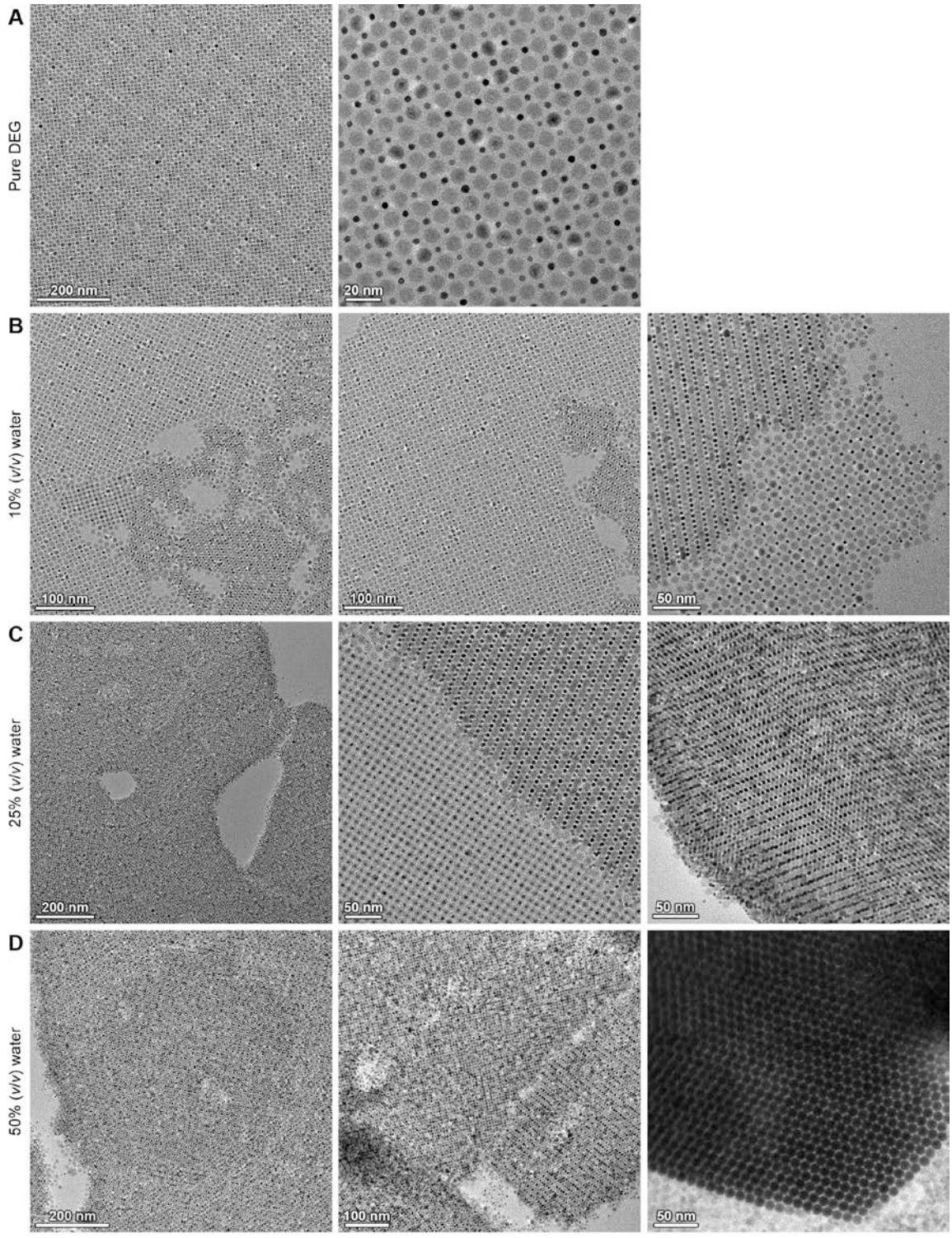

Fig. S51. Effect of the underlying liquid on Au-Fe_3O_4 BNSLs

Representative TEM images of NP superlattices obtained from the same 1:1 mixture of 5 nm Au NPs and 10 nm Fe_3O_4 NPs applied onto different liquids: (**A**) DEG, (**B**) 9:1 DEG-water, (**C**) 3:1 DEG-water, and (**D**) 1:1 DEG-water.

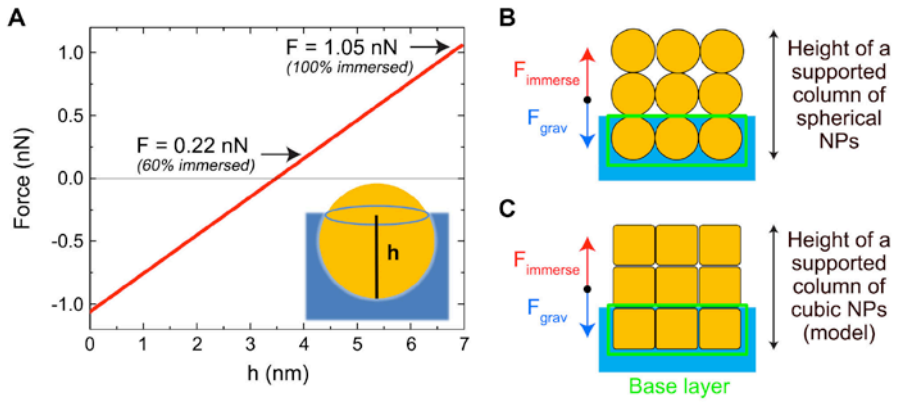

Fig. S52. Forces associated with the immersion of individual NPs and NP superlattices

(A) Net force acting on a dodecanethiol-functionalized spherical Au NP as a function of its immersion height in DEG. The NP has an effective diameter of 7 nm to account for the presence of dodecanethiol ligands on the gold core. The force is linearly dependent on height, giving a zero value for an approximately half-immersed NP (equilibrium) and a maximum value of 1.05 nN at 100% immersion. **(B)** Forces acting on a superlattice of self-assembled spherical NPs positioned at the DEG-vacuum interface (side view). Forces associated with the superlattice solvation ($F_{immerse}$) oppose immersion, while the gravitational force (F_{grav}) favors immersion. **(C)** The same analysis was used to examine a model superlattice formed by cubic NPs (see table S5).

System	**Interaction energy** (kcal/mol)
Au NP / DEG	–1,200
Fe_3O_4 NP / DEG	–4,450
Au NP / EG	–1,300
Fe_3O_4 NP / EG	–5,400
Au NP / H_2O	–400
Fe_3O_4 NP / H_2O	–1,900

Table S1.

Interaction energies (enthalpies) between individual NPs and DEG, EG, and water equilibrated at liquid-vacuum interfaces.

NP system	**Interaction energy** (kcal/mol)
Au-Au in vacuum	–250
Au-Fe_3O_4 in vacuum	–320
Fe_3O_4-Fe_3O_4 in vacuum	–480
Au-Au at the DEG-vacuum interface	–200
Au-Fe_3O_4 at the DEG-vacuum interface	–205
Fe_3O_4-Fe_3O_4 at the DEG-vacuum interface	–440

Table S2.

Interaction energies between NPs in NP pairs simulated in vacuum and at the DEG-vacuum interface.

	NPs per unit cell		*Contact types and their counts*					
BNSL	**Au**	**Fe_3O_4**	**Au-DEG**	**Fe_3O_4-DEG**	**Au-Au**	**Au-Fe_3O_4**	**Fe_3O_4-Fe_3O_4**	**E** (kcal/mol)
AB_4	8	2	4	1	9	20	0	17,900
AB_6	12	2	4	1	12	24	0	19,930
AB_{11}	22	2	4	1	50	24	1	29,910

Table S3.

Lattice energies of selected experimentally observed BNSLs.

Number of 7 nm NPs in the base layer	**Force required to immerse the base layer** (N)	**Gravitational force on the base layer** (N)	**Number of layers supported***	**Number of 7 nm NPs supported***	**Height of the supported column** (m)
1 x 1	$2.18 \cdot 10^{-10}$	$2.16 \cdot 10^{-20}$	$1.01 \cdot 10^{10}$	$1.01 \cdot 10^{10}$	70.6
7 x 7	$1.07 \cdot 10^{-8}$	$1.06 \cdot 10^{-18}$	$1.01 \cdot 10^{10}$	$4.95 \cdot 10^{11}$	70.6
71 x 71	$1.10 \cdot 10^{-6}$	$1.09 \cdot 10^{-16}$	$1.01 \cdot 10^{10}$	$5.09 \cdot 10^{13}$	70.6

Table S4.

Solvation and gravitational forces acting on superlattices assembled from spherical NPs at the DEG-vacuum interface. (*) The estimated numbers in columns 4 and 5 are obtained by assuming that the force required to immerse the system is equal to the gravitational force. The calculation of the forces required to immerse the system utilizes the dodecanethiol-DEG free energy of binding of $G° = -7$ kcal/(mol nm^2). For simplicity, it is assumed that the NPs are immersed only by 60% of their height. The blue row highlights a superlattice comprising ~$5 \cdot 10^{11}$ NPs, which is estimated to be the total number of NPs in our experimental system (estimated from experiments in which 10 μL hexane droplets containing 0.1 mg/mL of NPs are deposited onto DEG).

Size of the system's base (nm^2)	**Number of 7 nm NPs in the system's base**	**Force required to immerse the system** (N)	**Gravitational force on one "system NP"** (N)	**Number of "system NPs" supported**	**Number of 7 nm NPs supported***	**Height of the supported column**	**Number of 7 nm NPs in the immersed lattice**
1 x 1	1 x 1	$4.51 \cdot 10^{-10}$	$6.49 \cdot 10^{-20}$	$6.9416 \cdot 10^{9}$	$6.94 \cdot 10^{9}$	48.6 m	$6.94 \cdot 10^{9}$
50 x 50	7 x 7	$3.22 \cdot 10^{-9}$	$2.36 \cdot 10^{-17}$	$1.3605 \cdot 10^{8}$	$9.71 \cdot 10^{8}$	6.8 m	$4.8 \cdot 10^{10}$
500 x 500	71 x 71	$3.22 \cdot 10^{-8}$	$2.36 \cdot 10^{-14}$	$1.3605 \cdot 10^{6}$	$9.71 \cdot 10^{7}$	68 cm	$4.9 \cdot 10^{11}$
$5 \cdot 10^{3}$ x $5 \cdot 10^{3}$	714 x 714	$3.22 \cdot 10^{-7}$	$2.36 \cdot 10^{-11}$	$1.3605 \cdot 10^{4}$	$9.71 \cdot 10^{6}$	6.8 cm	$4.9 \cdot 10^{12}$
$5 \cdot 10^{4}$ x $5 \cdot 10^{4}$	7,140 x 7,140	$3.22 \cdot 10^{-6}$	$2.36 \cdot 10^{-8}$	$1.3605 \cdot 10^{2}$	$9.71 \cdot 10^{5}$	6.8 mm	$4.9 \cdot 10^{13}$
$5 \cdot 10^{5}$ x $5 \cdot 10^{5}$	71,400 x 71,400	$3.22 \cdot 10^{-5}$	$2.36 \cdot 10^{-5}$	$1.3605 \cdot 10^{0}$	$9.71 \cdot 10^{4}$	0.68 mm	$4.9 \cdot 10^{14}$

Table S5.

Solvation and gravitational forces acting on superlattices assembled from cubic NPs at the DEG-vacuum interface. (*) The estimated numbers in columns 5 and 6 were obtained assuming that the force required to immerse the system is equal to the gravitational force. The calculation of the solvation forces uses a scaled-down dodecanethiol-DEG free energy of binding, where $G° \sim -4.7$ kcal/(mol nm^2). The blue row highlights the superlattice comprising $\sim 5 \cdot 10^{11}$ NPs, which is estimated to be the total number of NPs in our typical experimental system.

Database S1.

The database includes electron tomography data and is publicly accessible under the links provided below.

- *vac*$_1$Au$_5$-type array:
  http://ematweb.uantwerpen.be/colouratoms/jsc3D/demos/vac1Au5.html
- *vac*$_1$Au$_{11}$-type array:
  http://ematweb.uantwerpen.be/colouratoms/jsc3D/demos/vac1Au11.html
- *vac*$_1$Au$_1$Au$_2$′Au″$_1$-type array:
  http://ematweb.uantwerpen.be/colouratoms/jsc3D/demos/vac1Au1Au2Au1.html
- *vac*$_1$Au$_1$Au′$_4$-type array:
  http://ematweb.uantwerpen.be/colouratoms/jsc3D/demos/vac1Au1Au4.html
- *vac*$_1$Au$_4$-type array:
  http://ematweb.uantwerpen.be/colouratoms/jsc3D/demos/vac1Au4.html
- *vac*$_1$Au$_1$-type array:
  http://ematweb.uantwerpen.be/colouratoms/jsc3D/demos/vac1Au1.html

References and Notes

1. E. V. Shevchenko, D. V. Talapin, N. A. Kotov, S. O'Brien, C. B. Murray, Structural diversity in binary nanoparticle superlattices. *Nature* **439**, 55–59 (2006). doi:10.1038/nature04414 Medline

2. N. A. Kotov, F. C. Meldrum, C. Wu, J. H. Fendler, Monoparticulate layer and Langmuir-Blodgett-type multiparticulate layers of size-quantized cadium-sulfide clusters—A colloid-chemical approach to superlattice construction. *J. Phys. Chem.* **98**, 2735–2738 (1994). doi:10.1021/j100062a006

3. S. Y. Park, A. K. R. Lytton-Jean, B. Lee, S. Weigand, G. C. Schatz, C. A. Mirkin, DNA-programmable nanoparticle crystallization. *Nature* **451**, 553–556 (2008). doi:10.1038/nature06508 Medline

4. Z. Tang, Z. Zhang, Y. Wang, S. C. Glotzer, N. A. Kotov, Self-assembly of CdTe nanocrystals into free-floating sheets. *Science* **314**, 274–278 (2006). doi:10.1126/science.1128045 Medline

5. D. Nykypanchuk, M. M. Maye, D. van der Lelie, O. Gang, DNA-guided crystallization of colloidal nanoparticles. *Nature* **451**, 549–552 (2008). doi:10.1038/nature06560 Medline

6. G. Singh, H. Chan, A. Baskin, E. Gelman, N. Repnin, P. Král, R. Klajn, Self-assembly of magnetite nanocubes into helical superstructures. *Science* **345**, 1149–1153 (2014). doi:10.1126/science.1254132 Medline

7. T. Wang, J. Zhuang, J. Lynch, O. Chen, Z. Wang, X. Wang, D. LaMontagne, H. Wu, Z. Wang, Y. C. Cao, Self-assembled colloidal superparticles from nanorods. *Science* **338**, 358–363 (2012). doi:10.1126/science.1224221 Medline

8. E. V. Shevchenko, M. Ringler, A. Schwemer, D. V. Talapin, T. A. Klar, A. L. Rogach, J. Feldmann, A. P. Alivisatos, Self-assembled binary superlattices of CdSe and Au nanocrystals and their fluorescence properties. *J. Am. Chem. Soc.* **130**, 3274–3275 (2008). doi:10.1021/ja710619s Medline

9. M. Ibáñez, Z. Luo, A. Genç, L. Piveteau, S. Ortega, D. Cadavid, O. Dobrozhan, Y. Liu, M. Nachtegaal, M. Zebarjadi, J. Arbiol, M. V. Kovalenko, A. Cabot, High-performance thermoelectric nanocomposites from nanocrystal building blocks. *Nat. Commun.* **7**, 10766 (2016). doi:10.1038/ncomms10766 Medline

10. A. Dong, J. Chen, X. Ye, J. M. Kikkawa, C. B. Murray, Enhanced thermal stability and magnetic properties in NaCl-type FePt-MnO binary nanocrystal superlattices. *J. Am. Chem. Soc.* **133**, 13296–13299 (2011). doi:10.1021/ja2057314 Medline

11. Y. Kang, X. Ye, J. Chen, Y. Cai, R. E. Diaz, R. R. Adzic, E. A. Stach, C. B. Murray, Design of Pt-Pd binary superlattices exploiting shape effects and synergistic effects for oxygen reduction reactions. *J. Am. Chem. Soc.* **135**, 42–45 (2013). doi:10.1021/ja3097527 Medline

12. J. J. Urban, D. V. Talapin, E. V. Shevchenko, C. R. Kagan, C. B. Murray, Synergism in binary nanocrystal superlattices leads to enhanced p-type conductivity in self-assembled PbTe/Ag_2 Te thin films. *Nat. Mater.* **6**, 115–121 (2007). doi:10.1038/nmat1826 Medline

13. M. P. Boneschanscher, W. H. Evers, J. J. Geuchies, T. Altantzis, B. Goris, F. T. Rabouw, S. A. P. van Rossum, H. S. J. van der Zant, L. D. A. Siebbeles, G. Van Tendeloo, I. Swart, J. Hilhorst, A. V. Petukhov, S. Bals, D. Vanmaekelbergh, Long-range orientation and atomic attachment of nanocrystals in 2D honeycomb superlattices. *Science* **344**, 1377–1380 (2014). doi:10.1126/science.1252642 Medline

14. H. Lin, S. Lee, L. Sun, M. Spellings, M. Engel, S. C. Glotzer, C. A. Mirkin, Clathrate colloidal crystals. *Science* **355**, 931–935 (2017). doi:10.1126/science.aal3919 Medline

15. A. M. Kalsin, M. Fialkowski, M. Paszewski, S. K. Smoukov, K. J. M. Bishop, B. A. Grzybowski, Electrostatic self-assembly of binary nanoparticle crystals with a diamond-like lattice. *Science* **312**, 420–424 (2006). doi:10.1126/science.1125124 Medline

16. C. J. Kiely, J. Fink, M. Brust, D. Bethell, D. J. Schiffrin, Spontaneous ordering of bimodal ensembles of nanoscopic gold clusters. *Nature* **396**, 444–446 (1998). doi:10.1038/24808

17. Y. Yu, C. A. Bosoy, D. M. Smilgies, B. A. Korgel, Self-assembly and thermal stability of binary superlattices of gold and silicon nanocrystals. *J. Phys. Chem. Lett.* **4**, 3677–3682 (2013). doi:10.1021/jz401964s Medline

18. T. Altantzis, Z. J. Yang, S. Bals, G. Van Tendeloo, M. P. Pileni, Thermal stability of $CoAu_{13}$ binary nanoparticle superlattices under the electron beam. *Chem. Mater.* **28**, 716–719 (2016). doi:10.1021/acs.chemmater.5b04898

19. Materials and methods are available as supplementary materials.

20. A. Dong, J. Chen, P. M. Vora, J. M. Kikkawa, C. B. Murray, Binary nanocrystal superlattice membranes self-assembled at the liquid-air interface. *Nature* **466**, 474–477 (2010). doi:10.1038/nature09188 Medline

21. Y. Jiao, D. Han, Y. Ding, X. Zhang, G. Guo, J. Hu, D. Yang, A. Dong, Fabrication of three-dimensionally interconnected nanoparticle superlattices and their lithium-ion storage properties. *Nat. Commun.* **6**, 6420 (2015). doi:10.1038/ncomms7420 Medline

22. E. V. Shevchenko, D. V. Talapin, C. B. Murray, S. O'Brien, Structural characterization of self-assembled multifunctional binary nanoparticle superlattices. *J. Am. Chem. Soc.* **128**, 3620–3637 (2006). doi:10.1021/ja0564261 Medline

23. H. Friedrich, C. J. Gommes, K. Overgaag, J. D. Meeldijk, W. H. Evers, B. de Nijs, M. P. Boneschanscher, P. E. de Jongh, A. J. Verkleij, K. P. de Jong, A. van Blaaderen, D. Vanmaekelbergh, Quantitative structural analysis of binary nanocrystal superlattices by electron tomography. *Nano Lett.* **9**, 2719–2724 (2009). doi:10.1021/nl901212m Medline

24. M. P. Boneschanscher, W. H. Evers, W. Qi, J. D. Meeldijk, M. Dijkstra, D. Vanmaekelbergh, Electron tomography resolves a novel crystal structure in a binary nanocrystal superlattice. *Nano Lett.* **13**, 1312–1316 (2013). doi:10.1021/nl400100c Medline

25. E. V. Shevchenko, D. V. Talapin, S. O'Brien, C. B. Murray, Polymorphism in $AB_{(13)}$ nanoparticle superlattices: An example of semiconductor-metal metamaterials. *J. Am. Chem. Soc.* **127**, 8741–8747 (2005). doi:10.1021/ja050510z Medline

26. V. Aleksandrovic, D. Greshnykh, I. Randjelovic, A. Frömsdorf, A. Kornowski, S. V. Roth, C. Klinke, H. Weller, Preparation and electrical properties of cobalt-platinum

nanoparticle monolayers deposited by the Langmuir-Blodgett technique. *ACS Nano* **2**, 1123–1130 (2008). doi:10.1021/nn800147a Medline

27. A. Dong, X. Ye, J. Chen, C. B. Murray, Two-dimensional binary and ternary nanocrystal superlattices: The case of monolayers and bilayers. *Nano Lett.* **11**, 1804–1809 (2011). doi:10.1021/nl200468p Medline

28. X. Ye, J. Chen, M. Engel, J. A. Millan, W. Li, L. Qi, G. Xing, J. E. Collins, C. R. Kagan, J. Li, S. C. Glotzer, C. B. Murray, Competition of shape and interaction patchiness for self-assembling nanoplates. *Nat. Chem.* **5**, 466–473 (2013). doi:10.1038/nchem.1651 Medline

29. Z. Yang, J. Wei, P. Bonville, M. P. Pileni, Beyond entropy: Magnetic forces induce formation of quasicrystalline structure in binary nanocrystal superlattices. *J. Am. Chem. Soc.* **137**, 4487–4493 (2015). doi:10.1021/jacs.5b00332 Medline

30. W. H. Evers, H. Friedrich, L. Filion, M. Dijkstra, D. Vanmaekelbergh, Observation of a ternary nanocrystal superlattice and its structural characterization by electron tomography. *Angew. Chem. Int. Ed.* **48**, 9655–9657 (2009). doi:10.1002/anie.200904821 Medline

31. T. Wen, S. A. Majetich, Ultra-large-area self-assembled monolayers of nanoparticles. *ACS Nano* **5**, 8868–8876 (2011). doi:10.1021/nn2037048 Medline

32. S. Stoeva, K. J. Klabunde, C. M. Sorensen, I. Dragieva, Gram-scale synthesis of monodisperse gold colloids by the solvated metal atom dispersion method and digestive ripening and their organization into two- and three-dimensional structures. *J. Am. Chem. Soc.* **124**, 2305–2311 (2002). doi:10.1021/ja012076g Medline

33. B. H. Wu, H. Y. Yang, H. Q. Huang, G. X. Chen, N. F. Zheng, Solvent effect on the synthesis of monodisperse amine-capped Au nanoparticles. *Chin. Chem. Lett.* **24**, 457–462 (2013). doi:10.1016/j.cclet.2013.03.054

34. T. Zdobinsky, P. S. Maiti, R. Klajn, Support curvature and conformational freedom control chemical reactivity of immobilized species. *J. Am. Chem. Soc.* **136**, 2711–2714 (2014). doi:10.1021/ja411573a Medline

35. J. Park, K. An, Y. Hwang, J. G. Park, H. J. Noh, J. Y. Kim, J. H. Park, N. M. Hwang, T. Hyeon, Ultra-large-scale syntheses of monodisperse nanocrystals. *Nat. Mater.* **3**, 891–895 (2004). doi:10.1038/nmat1251 Medline

36. A. E. Saunders, B. A. Korgel, Observation of an AB phase in bidisperse nanocrystal superlattices. *ChemPhysChem* **6**, 61–65 (2005). doi:10.1002/cphc.200400382 Medline

37. E. V. Shevchenko, D. V. Talapin, A. L. Rogach, A. Kornowski, M. Haase, H. Weller, Colloidal synthesis and self-assembly of $CoPt_3$ nanocrystals. *J. Am. Chem. Soc.* **124**, 11480–11485 (2002). doi:10.1021/ja025976l Medline

38. B. W. Goodfellow, M. R. Rasch, C. M. Hessel, R. N. Patel, D. M. Smilgies, B. A. Korgel, Ordered structure rearrangements in heated gold nanocrystal superlattices. *Nano Lett.* **13**, 5710–5714 (2013). doi:10.1021/nl403458q Medline

39. W. van Aarle, W. J. Palenstijn, J. De Beenhouwer, T. Altantzis, S. Bals, K. J. Batenburg, J. Sijbers, The ASTRA Toolbox: A platform for advanced algorithm development in

electron tomography. *Ultramicroscopy* **157**, 35–47 (2015). doi:10.1016/j.ultramic.2015.05.002 Medline

40. J. He, X. M. Lin, H. Chan, L. Vuković, P. Král, H. M. Jaeger, Diffusion and filtration properties of self-assembled gold nanocrystal membranes. *Nano Lett.* **11**, 2430–2435 (2011). doi:10.1021/nl200841a Medline

41. M. K. Bera, H. Chan, D. F. Moyano, H. Yu, S. Tatur, D. Amoanu, W. Bu, V. M. Rotello, M. Meron, P. Král, B. Lin, M. L. Schlossman, Interfacial localization and voltage-tunable arrays of charged nanoparticles. *Nano Lett.* **14**, 6816–6822 (2014). doi:10.1021/nl502450j Medline

42. H. Zhao, S. Sen, T. Udayabhaskararao, M. Sawczyk, K. Kučanda, D. Manna, P. K. Kundu, J.-W. Lee, P. Král, R. Klajn, Reversible trapping and reaction acceleration within dynamically self-assembling nanoflasks. *Nat. Nanotechnol.* **11**, 82–88 (2016). doi:10.1038/nnano.2015.256 Medline

43. J. C. Phillips, R. Braun, W. Wang, J. Gumbart, E. Tajkhorshid, E. Villa, C. Chipot, R. D. Skeel, L. Kalé, K. Schulten, Scalable molecular dynamics with NAMD. *J. Comput. Chem.* **26**, 1781–1802 (2005). doi:10.1002/jcc.20289 Medline

44. K. Vanommeslaeghe, E. Hatcher, C. Acharya, S. Kundu, S. Zhong, J. Shim, E. Darian, O. Guvench, P. Lopes, I. Vorobyov, A. D. Mackerell Jr., CHARMM general force field: A force field for drug-like molecules compatible with the CHARMM all-atom additive biological force fields. *J. Comput. Chem.* **31**, 671–690 (2010). Medline

45. W. Yu, X. He, K. Vanommeslaeghe, A. D. MacKerell Jr., Extension of the CHARMM General Force Field to sulfonyl-containing compounds and its utility in biomolecular simulations. *J. Comput. Chem.* **33**, 2451–2468 (2012). doi:10.1002/jcc.23067 Medline

46. K. Vanommeslaeghe, A. D. MacKerell Jr., Automation of the CHARMM General Force Field (CGenFF) I: Bond perception and atom typing. *J. Chem. Inf. Model.* **52**, 3144–3154 (2012). doi:10.1021/ci300363c Medline

47. K. Vanommeslaeghe, E. P. Raman, A. D. MacKerell Jr., Automation of the CHARMM General Force Field (CGenFF) II: Assignment of bonded parameters and partial atomic charges. *J. Chem. Inf. Model.* **52**, 3155–3168 (2012). doi:10.1021/ci3003649 Medline

48. T. Darden, D. York, L. Pedersen, Particle mesh Ewald: An N·log(N) method for Ewald sums in large systems. *J. Chem. Phys.* **98**, 10089–10092 (1993). doi:10.1063/1.464397

49. W. Humphrey, A. Dalke, K. Schulten, VMD: Visual molecular dynamics. *J. Mol. Graph.* **14**, 33–38, 27–28 (1996). doi:10.1016/0263-7855(96)00018-5 Medline

50. L. Vuković, A. Madriaga, A. Kuzmis, A. Banerjee, A. Tang, K. Tao, N. Shah, P. Král, H. Onyuksel, Solubilization of therapeutic agents in micellar nanomedicines. *Langmuir* **29**, 15747–15754 (2013). doi:10.1021/la403264w Medline

51. A. Grossfield, WHAM: The weighted histogram analysis method (University of Rochester Medical Center, 2012); accessed April 2017.

52. S. Kumar, J. M. Rosenberg, D. Bouzida, R. H. Swendsen, P. A. Kollman, The weighted histogram analysis method for free-energy calculations on biomolecules. I. The method. *J. Comput. Chem.* **13**, 1011–1021 (1992). doi:10.1002/jcc.540130812